UoA

Undergraduate Mechatronics Research Journal

Volume 1 • December 2008

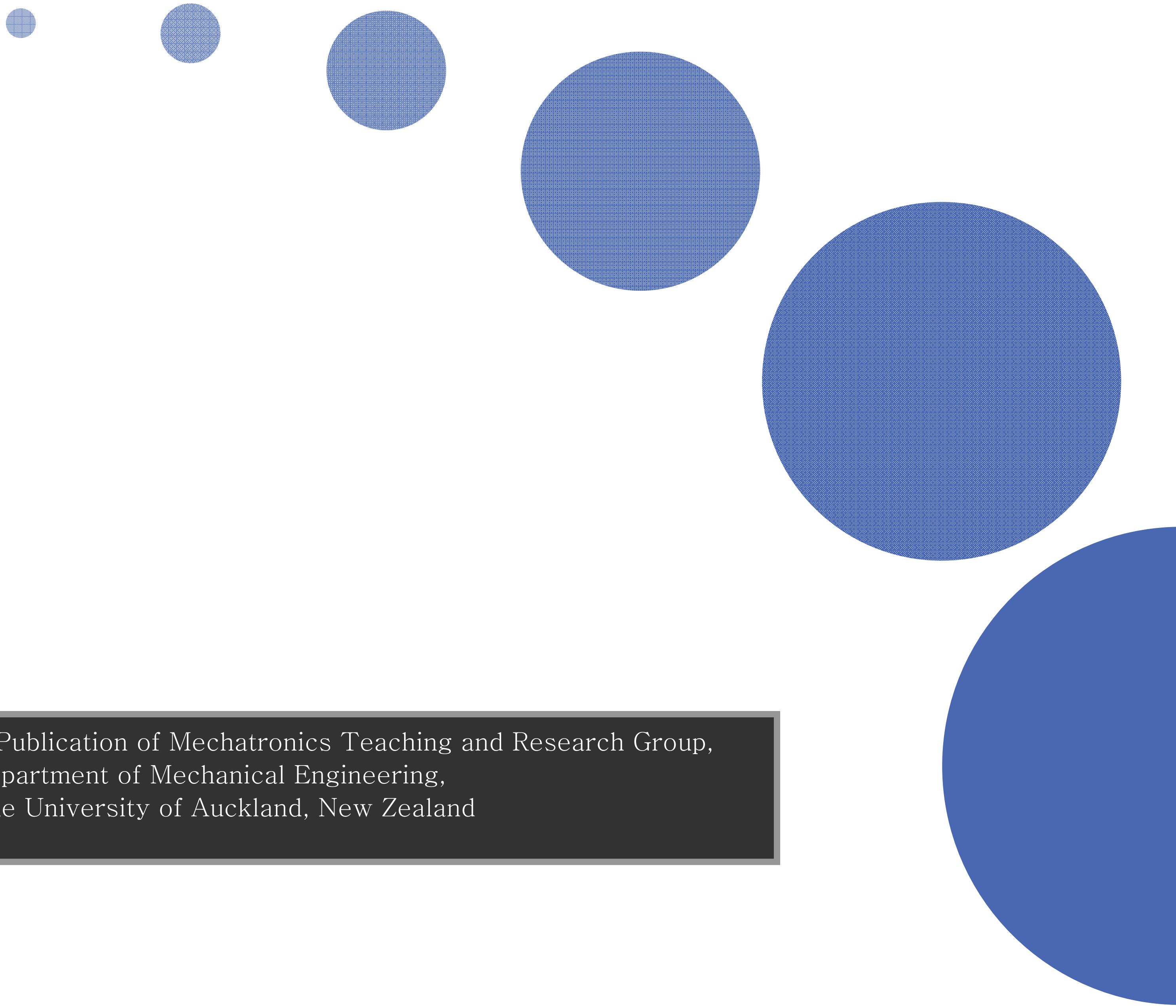

A Publication of Mechatronics Teaching and Research Group,
Department of Mechanical Engineering,
The University of Auckland, New Zealand

ISSN 1171-9494

UoA Undergraduate Mechatronics Research Journal

UoA Undergraduate Mechatronics Research Journal is published annually by the Mechatronics Teaching and Research Group of the Mechanical Engineering Department, The University of Auckland, 20, Symonds Street, Auckland, New Zealand.

Preface

Welcome to University of Auckland Undergraduate Mechatronics Research Journal. This is the inaugural publication (Vol. 1) of undergraduate papers from the mechatronics engineering students derived from their final year (senior) projects. The journal offers undergraduates the chance to share and express their engineering concepts and achievements and will be published annually.

Undergraduate students from mechatronics engineering are invited to submit papers outlining the process and results of their mechatronics research or scholarly/creative activity conducted during their final year (senior) project. We also encourage students to submit their summer internship or postgraduate project papers, etc for possible publication in this journal. The submissions to the journal will be structured and organised or sectioned in a manner that maximises both the substance and clarity of the document. All submitted manuscripts will be reviewed to ensure that only good science/engineering will be published in the journal.

Finally, I like to thank all reviewers and editors for providing feedbacks and comments.

KEAN C. AW
Editor-in-Chief

Table of Contents

RESEARCH ARTICLE

REVIEW ARTICLE

The Undergraduate Mechatronics Research Journal , Vol. 1

RESEARCH ARTICLE

Implementation of an Intelligent Obstacle Avoidance System using a Single Ultrasonic Sensor

James Pau, Arief Probo Tjahyono
The University of Auckland,
Department of Mechanical Engineering,
Mechatronics Engineering,
New Zealand

Abstract

This article documents the implementation of an obstacle avoidance system for an autonomous vehicle that uses a single ultrasonic sensor. The system is built around an adaptation of the enhanced vector polar histogram algorithm (VPH+) which was originally developed for a laser rangefinder. The testing rig used to test the performance of the adapted algorithm was an autonomous guided vehicle (AGV) developed by the Mechanical Engineering Department of the University of Auckland as a long term project for final year undergraduate students.

The algorithm introduced a new ability to the AGV and allowed it to avoid obstacles 'on-the-fly' with time efficient turning operations. Tests and trial runs found that the AGV could handle both simple and complex scenarios with a satisfying degree of accuracy. A significant drawback however was found in that the AGV could not avoid objects with angled surfaces.

Keywords: *Autonomous Guided Vehicles; Enhanced Vector Polar Histogram; FPGA*

1. Introduction

The Mechanical Engineering Department of the University of Auckland has been developing a low cost autonomous guided vehicle (AGV) since 2005. This uses global path planning and local obstacle avoidance techniques to navigate from one predetermined waypoint to another, without the input of a human operator. The AGV uses a single ultrasonic sensor to detect obstacles and this is the main limiting factor in its ability to detect and avoid obstacles.

The 2007 project group's obstacle avoidance algorithm, OASYS, was primitive and basic in its structure. Because the sensor was rigidly fixed to the AGV, it used a simple step-by-step decision making process where the AGV would stop and rotate on the spot to find a clear path. Although successful at finding ways around obstacles, the algorithm was time inefficient and did not have any form of planning to find the optimal path.

Obstacle avoidance algorithms have been developing since the early 1980s and have undergone numerous changes and improvements. The most recent is the enhanced vector polar histogram algorithm (VPH+) and is built using principles developed from previous algorithms [1]. This was implemented on a mobile robot with a laser rangefinder and found to be very time efficient and effective at navigating through complex scenarios at reasonable speeds.

The aim of the 2008 project was to develop a robust obstacle avoidance system to allow a low cost vehicle with a single ultrasonic sensor to avoid obstacles 'on-the-fly'. This was done by adapting the VPH+ algorithm to work with an ultrasonic sensor.

2. Adaptation and Implications

A laser range finder has a 180° field of view and can potentially identify 181 distinct points where an object might be, giving a scanning width resolution of 1° [1]. The scanning range can be up to 5300 mm [2] and the sensor remains stationary for its scans. An ultrasonic sensor on the other hand has a scanning width resolution of 26° and maximum scanning range of 1300 mm. If the sensor is to scan over a 180° angle, it must be moved physically. This is done by mounting the ultrasonic sensor onto a stepper motor.

The VPH+ algorithm was developed for a laser range finder and will therefore encounter difficulties when implemented with an ultrasonic sensor. Noise will easily confuse the vehicle as echoes can affect distance measurements. Also, because the scanning width is so wide, the sizes of obstacles detected are misrepresented. This means that possible clear paths will not be detected and the vehicle will not always travel along a sensible path, purely because it cannot find it. Laser sensors also have a scanning frequency up to 2500 Hz [2] and can thus continuously scan and analyse the environment many times a second. In contrast, a mobilised ultrasonic sensor requires time to move to different position to obtain the necessary data. This is a time consuming process and is undesirable as the robot will be continuously moving forward and unable to react quickly to the environment. As a result of the longer planning cycle, the speed of the vehicle will need to be much slower in order for it to have time to react to its surroundings.

The environment that the vehicle operates in must be static. If the environment is dynamic and the obstacles are in motion, collisions will be highly likely because any course of action the vehicle decides to take will be in a situation that has since changed and therefore the decision will be rendered ineffective and inaccurate.

3. Adapted Algorithm Steps

Step 1 – Finding Maximum Reachable Distances

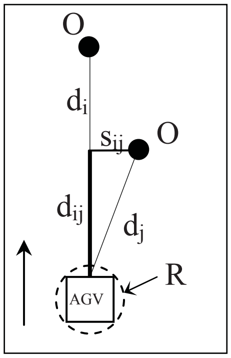

Figure 1. Diagram of the maximum reachable distance

This is the first step of the algorithm, calculating the maximum reachable distance for a particular obstacle. Figure 1 illustrates the first step where O_i and O_j represent obstacles having a distance of d_i and d_j respectively from the AGV. The perpendicular distance between O_i and O_j is S_{ij}, calculated using equation 1 where *i* is the sector of interest, *j* is the neighbouring sector and α is the angle between sectors.

$$s_{ij} = d_j \sin(\propto) \tag{1}$$

The maximum reachable distances of the sector of interest, d_{ij}, are then calculated using equation 2, where the radius of the vehicle with a safety factor applied, *R*, is taken into consideration. The maximum reachable distance of the sector of interest is found by finding the smallest value of d_{ij} and subtracting *R* from it, given in equation 3.

$$d_{ij} = \begin{cases} d_i & s_{ij} > R \text{ or } (s_{ij} < R \text{ and } d_j \cos(\alpha) > d_i) \\ d_j \cos(\alpha) & \text{otherwise} \end{cases} \tag{2}$$

$$D_i = \min(d_{ij}) - R \tag{3}$$

Step 2 – Obstacle Block Grouping and Symbol Function

This step of the algorithm groups detected obstacles into blocks and then converts them into a binary output based on whether the blocks are concave or non-concave. It does this by taking the distance readings of the sectors and comparing the distances between adjacent sectors using equation 4.

$$d_{i,i+1} = \sqrt{d_i^2 + d_{i+1}^2 - 2d_i d_{i+1}\cos(\alpha)} \quad (4)$$

$$B_i = \begin{cases} 0 & \text{obstacle in sector } i \text{ belongs to a concave block} \\ 1 & \text{otherwise} \end{cases} \quad (5)$$

The result is compared to a threshold distance, d_{thr}, which determines what size gap between obstacles is acceptable to consider them separate. If $d_{i,i+1}$ is less than d_{thr} the vehicle cannot fit between the neighbouring obstacles and the obstacles can therefore be considered as one – or an obstacle block. The next process is to establish the concavity nature of each block by comparing the end points of each obstacle block. A binary value, B_i, is assigned for each sector to represent its concavity of the obstacle present in it, shown in equation 5.

Step 3 – Threshold Function

The third step of the algorithm calculates a safe distance, d_{safe}, which is the minimum distance an object must be to avoid a collision during the next planning cycle, i.e. while the vehicle is determining where to go next. The value of d_{safe} depends on the minimum turning radius of the vehicle (R_{min}), the maximum speed (v_{max}), the current speed (v) and the time taken by each planning cycle (T), shown in equation 6.

$$d_{thr} = K\left(\frac{v}{v_{max}} R_{min} + vT\right) \quad (6)$$

K is the safety factor and can be a value from 1.2 to 1.5. However, because the speed of the vehicle will be kept constant at v_{max}, equation 6 becomes equation 7.

$$d_{thr} = K\left(R_{min} + v_{max}T\right) \quad (7)$$

The threshold function checks the maximum reachable distance of each sector (calculated in Step 1) against d_{safe} and assigns binary values to an array, H, based on the following criteria:

$$H_i = \begin{cases} 1 & D_i > d_{thr} \\ 0 & otherwise \end{cases} \quad (8)$$

Step 4 – Cost Function

The last step of the algorithm uses all the calculations done in previous steps to determine the best path to take in order to avoid the obstacle. It uses equation 9 to calculate the cost of travelling to each sector where the sector with the highest cost is the most optimal path for a given set of readings. The numerator consists of binary values from the symbol and threshold functions where a value of 0 from any of those function would disable the sector, returning a cost value of 0. Otherwise, the cost is calculated using the maximum reachable distance and the denominator, S_i, a goal oriented value that is derived from equation 10. The output of the cost function is the index of the sector with the highest cost.

$$C_i = \frac{B_i H_i D_i}{S_i} \quad (9)$$

$$S_i = k_1 h_g + k_2 h_o + k_3 \quad (10)$$

Each term in equation 10 is associated with the current heading of the vehicle. The first term, $k_1 h_g$, is associated with the angle between the goal point and the obstacle and the second term, $k_2 h_0$, is associated with the angle between the obstacle and current heading. As the time taken to reach the goal point is to be minimised, the first term has a higher priority resulting in constant k_1 to be greater than constant k_2. The constant k_3 ensures that the denominator is always greater than zero. The vehicle's current heading is used as a reference for the calculated deviation error where positive values are assigned for the errors to the right of the AGV and negative for the errors to the left.

4. Experimental Set-Up

The adapted algorithm was programmed onto the AGV developed in the University of Auckland, shown in Figure 2(a). An ALTERA DE2 Development and Evaluation board is a field programmable gate array (FPGA) board and was used to control the AGV. The AGV was configured to use five sectors with each set apart 30° because this was the closest and simplest angle to the ultrasonic scanning angle of 26°. This means that the sensor is rotated 120° and has a total scanning angle close to 150°. A small 8° blind spot forms between the sectors as a result of this and at the full scanning range of 1300 mm, the undetected distance is 180 mm. However, because the objects being used as obstacles are cardboard boxes and tables, which are larger than 400 mm, the effects of the blind spots in the testing environment were considered negligible. Figure 3(a) shows the arrangement of the sectors used for testing the AGV and the blind spots in between. The available sectors also represent the possible turning directions of the AGV and having five sectors mean there are two possible turning angles on each side – a 30° or 60° turn.

The parameters v_{max} and R_{min} were estimated to be 150 mm/s and 250 mm respectively because they would have been difficult to measure. Since their only effect was on the threshold distance and the speed of the AGV was not being varied, these estimations were acceptable. The values for k_1, k_2, and k_3 were chosen to be 5, 3 and 2 respectively and kept constant throughout the trials. The behaviour of the AGV was able to be monitored through the console output on a laptop and a video of the test run. By matching the output to the actions taken in the video, the AGV's reasoning could be analysed and reasons for particular incidents or collisions could be determined.

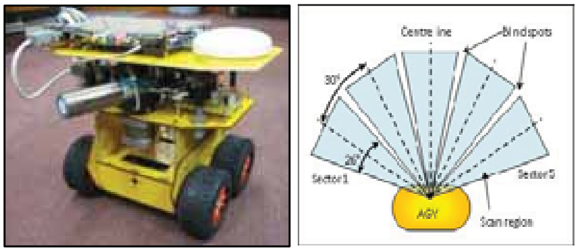

(a) The complete AGV (b) The sector layout

Figure 2. Autonomous guided vehicle developed in The University of Auckland

5. Experimental Results and Discussions

Scenario 1 uses a simple layout for the obstacle to be avoided by the AGV. This scenario was used to test the adaptability of the VPH+ algorithm to an ultrasonic sensor. As shown by Figure 3(a), the AGV avoided the boxes successfully, which suggested that the concept of using the VPH+ algorithm with an ultrasonic sensor does work.

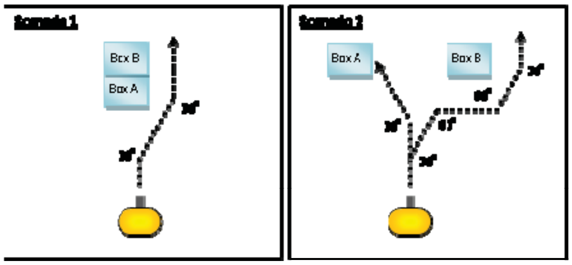

(a) Scenario 1 (b) Scenario 2

Figure 3. Experimental Results for scenario 1 and 2

Further trials using different scenarios with more difficult layout were done. These trials allowed the algorithm's parameters to be fine tuned and the system to be debugged. This was done for scenario 2, 3 and 4 where the AGV's radius used in equation 3, R, was adjusted to 190 mm from the 160 mm radius initially used.

Figure 3(b) illustrates the result obtained from scenario 2 where two obstacles were used. As illustrated, one path shows a successful obstacle avoidance while the other shows a collision with one of the obstacles. This is contributed to the noisy readings, which are very dependent on the surroundings, from the ultrasonic sensor.

Scenario 3 represents a situation where the AGV has to go through an opening such as a doorway, with the result shown in Figure 4(a). The AGV identified the opening and successfully passed through it, illustrated by the dashed line.

Scenario 4 was laid out for continuous obstacle avoidance using boxes and a table as the obstacles. Shown in Figure 4(b), the AGV avoided the obstacles by selecting the only collision-free path available. This trial also shows that obstacles with different surface types could be detected.

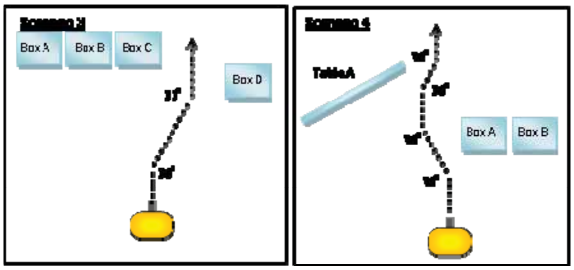

(b) Scenario 3 (b) Scenario 4

Figure 4. Experimental Results for scenario 3 and 4

Overall, 27 successful trials were obtained from a total of 40 trials. The majority of the unsuccessful trails were caused by the low quality signals (reflected sound waves) received by the ultrasonic sensor. As the surface angle of the obstacle and the ultrasonic sensor are not always perpendicular to each other, the sound waves may be directed away from the ultrasonic sensor. This causes the readings to be incorrect and provides the algorithm with false information. This proves that the adapted algorithm does indeed work.

6 Conclusions

An adapted VPH+ algorithm was successfully implemented and tested on a more primitive platform than what it was originally developed for. The algorithm was fed data obtained from a mobile ultrasonic sensor instead of a laser rangefinder and was able to guide our AGV around obstacles, in simple and complex situations.

The performance of the algorithm was acceptable. During trials it was found that the algorithm was doing what it could with the data provided to it. Collisions of the vehicle and any other seemingly irrational behaviours were attributed to noisy readings from the ultrasonic sensor. The algorithm was not able to perform well with obstacles that were angled because the sensor was not detecting these obstacles at all. The scenarios with angled boxes were where most of the collisions occurred.

Acknowledgement

Special thanks to Dr K.C. Aw and Mr Ken Snow for their contribution in this project.

References

1. Gong, J., Duan, Y., Man, Y., & Xiong, G. (2007). VPH+: An Enhanced Vector Polar Histogram Method for Mobile Robot Obstacle Avoidance. IEEE Conference on Mechatronics and Automation (Harbin), 2784-2788.
2. Klaassen, D. (2007). GPS Guided Autonomous Vehicle with Obstacle Avoidance System. 4th Year Project MT-17, Department of Mechanical Engineering, The University of Auckland.

Introducing Computer Control in Recreational SCUBA Diving

Jenny Xu, Anatoly Kudryashov
Department of Mechanical Engineering,
Mechatronics Engineering,
The University of Auckland, New Zealand

Abstract
The most important task for a diver is buoyancy control which determines the velocity and direction of travel while underwater. To date, control is carried out manually by regulating the amount of gas in the buoyancy control device (BCD). Unreliable buoyancy control exposes the diver to risks of injury and death. A control system was designed and manufactured at the University of Auckland, New Zealand to attach to the BCD and automatically adjust the diver's buoyancy to keep velocity and depth to safe levels. A pressure sensor was used to obtain current diver parameters and linear actuators were used to push valve control buttons on the BCD for air regulation. The control program was developed in C language and controller performance was verified through laboratory and real life testing. Successful results obtained show effective control of diver buoyancy when required.

Keywords: *Computer control; Scuba diving; Buoyancy*

1. Introduction

The buoyancy control device (BCD) is a crucial piece of recreational scuba diving equipment and enables divers to adjust their buoyancy under water to achieve desired movement. The BCD is essentially an inflatable jacket which is filled or deflated by the diver using push buttons. A low pressure direct feed transports gas from the diving cylinder via diving regulator to the device while purge valves positioned about the jacket allow gas to escape into the surrounding water.

Buoyancy control is a difficult process and if not managed properly may lead to rapid ascension or unsafe depths, both of which pose major health risks to the diver. In fact, the Divers Alert Network (DAN) 2005 Annual Review of Scuba Diving Injuries and Fatalities links up to 45% of fatal accidents with buoyancy problems. [1]

Thus, an onboard control system which can be attached to existing diving gear and which will help keep diver depth and velocity to within safe levels through active buoyancy control would greatly benefit divers by increasing overall safety in recreational scuba diving.

The BCD used as the basis for design and on which the produced prototype controller was attached for testing is made by DACOR and is currently one of the most popular models used by scuba divers.

2. Approach

The most simplistic and flexible approach is to use the existing manual push buttons to carry out buoyancy control. Manual control on the BCD uses two push buttons, one for opening the inlet valve for inflation and the other for opening the outlet valve for deflation. The idea is to implement a controller which will physically push these buttons by means of mechanical actuation in order to adjust the buoyancy of the diver accordingly. To do this, two actuators (one for each button) are required. For the controller to activate the correct actuator at the right time, it must know the current velocity and depth of the diver. This information can be obtained with the use of a pressure sensor.

3. Hardware Development

Component Selection

The ATmega8 microcontroller by ATMEL was used to pass and process information and induce desired control actions.

The pressure sensor used was 19C100 of the stainless Pressure Sensor cell series with a working range of up to 100 PSI which is equivalent to a depth of approximately 70 m underwater. [2] This is more than sufficient as recreational scuba divers never exceed the maximum depth of 40m during dives.

Voltage output from the pressure sensor is in millivolts and much too small to be read effectively by the microcontroller due to limited resolution of the ADC. An amplifier circuit was created to apply a gain of 100 to pressure sensor signals before passing the information to the microcontroller ADC.

Micro linear actuators by Firgelli were selected to push the valve buttons to regulate air in the BCD. The small displacement caused by button depression means the minimum stroke length of 10 mm for the chosen L12 series can be used. Through experimentation, it was found that 25-30 N of force was required to activate each button. The selected linear actuators were suitable as they provide up to 50 N of force each. [3]

An actuator driver was required as output signals from the microcontroller were insufficient to drive the linear actuators directly. The Solarbotics Compact L298 Motor Driver solves this problem and drives the actuators as well as controls the direction of actuation.

Figure 1 shows assembled components inside the designed controller housing.

Housing Design

Figure 1. Assembled Controller

A controller housing had to be designed and manufactured to accommodate all hardware components and circuitry. The housing had to be shaped as to complement the existing manual control unit on the BCD and allow linear actuators to act on the push buttons. An important consideration was the desire to still allow the diver to carry out manual control. This means that the push buttons must be exposed to give diver access and that the linear actuators will have to extend out of the controller housing to reach them. The final housing design and drawings were produced with the aid of CAD software Pro/Engineer Wildfire 4.0. The material used for manufacture was standard grey PVC due to its applications in pipe, plumbing and conduit fixtures which highlights its suitability for use in products dealing with water.

User Interface

The control panel placed on the housing lid serves as the user interface for the control system. There are three buttons present, the green power button, the blue depth mode button and the red emergency button as shown in Figure 2.

Figure 2. Control Panel on Housing Lid

Switching on the power button supplies the entire control system with power from two rechargeable 12 V lithium batteries with ratings of 1320 mAh. These are able to drive the system for up to 60 minutes which is sufficient as average dive times range between 35-45 minutes. When the depth button is activated, the controller is prompted to enter ‘cruise control’ mode in which the diver’s current depth is recorded and buoyancy adjusted to maintain the set depth. The emergency button deactivates the controller by retracting both linear actuators to give the diver full manual control. The pressure sensor used is exposed to the surrounding water and can also be seen on the control panel.

Waterproofing

Waterproofing was a major issue as the controller will be operating under water for extended periods of time. This was made more difficult as linear actuators were required to move in and out of the housing. Figure 3 indicates the final water proofing precautions taken for the housing body.

Figure 3. Water Proofing the Housing Body

Flexible rubber sleeves were used to allow for actuator movement. An O-ring was inserted between the housing base and lid to create a water tight seal when the two parts were bolted together. Finally, silicon sealant was used to ensure all gaps have been properly sealed.

Waterproofing of the control panel on the housing lid was achieved by using water proof caps for all buttons and using silicon sealant to close any gaps. An O-ring was placed at the base of the pressure sensor to create a water seal when the sensor was screwed in tightly.

Clamp Design

A clamp assembly was designed in order to attach the controller unit to the diver BCD securely and ensure it remains stationary with respect to the manual unit so the linear actuators are lined up with the appropriate push buttons. Pro/Engineer Wildfire 4.0 was also used for design and standard grey PVC used for manufacture.

4. Software Development

Controller Type

A simple ‘On-Off’ controller was selected for implementation. This was appropriate for use in this application as response times were expected to be relatively slow.

Controller Program

The controller program was developed in C language on the PC and written directly to the microcontroller through the ISP port via the DonKey USB connector. The ADC interrupt was utilized to continuously check the current parameters of the diver to determine whether any control actions were needed. The initialisation at the start of the program sets up the output, input and ADC ports of the ATmega8 microcontroller as required.

The output port is responsible for sending signals to the motor driver to activate the correct linear actuator at the appropriate times. The inlet valve actuator is extended to pump gas into the BCD when the diver is sinking too fast or has dropped below the desired depth. Similarly, the outlet valve actuator is extended to purge air when the diver is ascending too fast or has risen above the desired depth.

The ADC port is set up so discrete pressure sensor voltage output can be read. By applying the mathematical relationship found through calibration, the depth of the diver can be calculated from this information. The velocity can then be obtained by checking the change in depth between subsequent samples given a constant sampling rate.

The input port is where the controller switches from the user interface are connected. The state of this port is continuously checked every time the ADC interrupt occurs. If a switch is turned on, the associated pin at the port will be grounded and will alert the microcontroller to enter the correct mode of operation. Once power is supplied to the control system, velocity control is carried out automatically. The depth button prompts the controller to enter the depth control mode to keep the diver at the depth registered when the mode was first entered. Switching off the button will reset the desired depth until the next time the button is activated. Turning on the emergency button causes the controller to retract both linear actuators and enter manual control mode. The controller then returns to its previous mode of operation when the emergency button is deactivated.

Safety Features

Velocity control is still active during depth control mode and takes precedence when action is required as high rates of ascension or fall poses a much more serious health risk than not being able to maintain a constant depth. Another safety feature is the monitoring of battery state by regularly checking pressure sensor voltage. This is important as low battery can cause erroneous controller actions. If low battery state is detected, the controller is prompted to enter manual control mode.

5. Calibration and Testing

Sensor Calibration

The pressure sensor and amplifier voltage outputs were calibrated to ensure linearity for the set working range (up to 20m underwater) of the prototype controller. The amplifier was set to cut off at 4V which corresponds to the upper limit of the working range and also allows a greater resolution to be achieved at the ADC due to a smaller input range compared to the usual 5V. Calibration was carried out using the Budenberg Dead Weight machine as well as using variable air pressure to ensure accuracy. Equation (1) obtained describes the relationship found between the diver's current pressure, P_{sensor} and the amplified pressure sensor voltage, V.

$$P_{sensor} = \frac{V - 1.3789}{1.8647} \qquad (1)$$

Diver depth z can then be calculated from the pressure by using equation (2) and diver velocity found by monitoring the change in depth.

$$z = \frac{P_{sensor} - P_{atm}}{\rho_w g} \qquad (2)$$

Where P_{atm} is the atmospheric pressure, ρ_w is the density of water and g is the acceleration due to gravity.

Laboratory Testing

Testing of the controller was initially carried out by connecting the pressure sensor to a variable air supply at the Manufacturing Laboratory of the Mechanical Engineering Department at the University of Auckland. Diver motion was simulated by varying the pressure applied to induce the correct controller responses. The full set up is shown in Figure 4.

Figure 4. Laboratory Testing Set Up

An air cylinder was also connected to the BCD so controller actions will be evident through the physical inflation and deflation of the jacket.

Real Life Testing

Real life testing of the prototype controller took place at the Olympic swimming pool in Newmarket, Auckland. All three modes of velocity, depth and manual control were test at this 4.7m deep pool. Figure 5 shows underwater testing of the controller.

6. Results and Conclusions

Both laboratory and real time testing verified controller performance by providing the correct controller actions when required. A successful prototype buoyancy controller was produced which actively limited the diver's velocity and depth to desired levels.

Figure 5. Underwater Testing

Acknowledgement

We would like to thank our supervisor A/Prof. Vojislav Kecman, our technician Mr. Robert Earl and Mr. Joel Glass from the workshop for their support. We would also like to acknowledge Mr. John Nixon from the Olympic Pool for letting us use the facilities.

References

1. Report on Decompression Illness, Diving Fatalities and Project Dive Exploration (2005). Divers Alert Network (DAN), 90.
2. Temperature compensated stainless steel Pressure Sensor cells 19C series (Undated). SenSym, SensorTechnics, Germany.
3. Miniature Linear Motion Series L12 (Undated). Firgelli Technologies Inc, Victoria, Canada.

The UoA Undergraduate Mechatronics Research Journal , Vol. 1

Development of a Multi-fingered Robotic Hand

I-Ching Lin, Theresa Lin
The University of Auckland,
Department of Mechanical Engineering,
Mechatronics Engineering,
New Zealand

Abstract

A multi-fingered robotic hand is developed using hydraulic actuation with fluidic actuators. A miniaturised hydraulic system is designed with all components intrinsically placed inside the palm. All finger parts of the prototype are integrated into a single unit and constructed from two part urethane mould, which is a very flexible material. Fourteen finger joints with 14 DOF are powered by fluidic actuators, which bend when hydraulic pressure is applied by the miniature water pump. The hand is designed to be under-actuated with only five degrees of controlled motion. Controlled by a programmed microcontroller, the hand can be operated under either automatic or manual mode. In the automatic mode, objects are gripped automatically when force sensors on the hand detect contact with objects. The gripping force is controlled by varying the PWM duty cycle outputted by the microcontroller. The hand is able to apply a power grip to grasp a 700g mass.

Keywords: *Robot hands; Hydraulic actuating system; Adaptive grasping*

1. Introduction

Hands are the chief organs for humans to achieve daily living tasks. They can perform fine, detailed movements or rough, forceful gripping motions. They are also the main tools for performing sensory functions, such as temperature and tactile feedbacks to the brain, which controls different reactions of human bodies [1].

As robotic technology grows, it is now possible for a robotic end-effecter to complete simple tasks that are usually done by humans. Repetitive assembly works can be done by robotic manipulators instead of human operators to speed up production [2]. This technology also has medical applications. Operation and rehabilitation robots can replace human hands to avoid hand vibration or other factors, especially when a steady and precise movement is required. Another new approach is to have humanoid robotic parts as prosthesis for amputees that have lost their limbs to regain their living abilities.

This project develops a prosthetic robotic hand.

The objectives of the proposed hand are:

1. The hand should have a humanoid appearance, i.e. the size, shape, and skin texture should be similar to a human hand.
2. The hand should be able perform human actions such as gripping, pitching, and pointing.
3. The hand should be portable. This means a light intrinsic design (i.e. any parts that are related to the functions of the hand should be embedded within the hand) is essential.
4. The hand should be controlled by an embedded controller with real time sensory feedback.

2. Miniaturised Hydraulic System

A miniaturised hydraulic system has been developed to actuate the finger joints. The concepts presented in the Fluidic hand using miniaturized hydraulic systems offer a very compact design. However, it lacks a suitable method for controlling the gripping force. Our design is based on a similar hydraulic system, but further improving it by introducing grip force control. The overall design of the hydraulic system is illustrated in Figure 1. The main components of the system include a water pump, a proportional flow and a manifold with five solenoid valves.

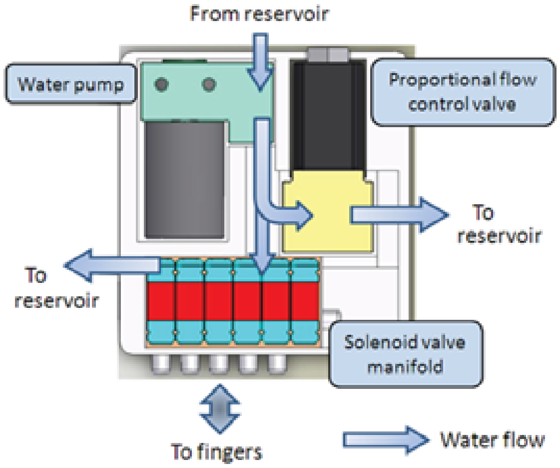

Figure 1. Flow diagram of the hydraulic system

A micro diaphragm liquid pump from KNF is used to pressurise water in the system to 6 bars. The proportional flow control valve from Burkert is used as a pressure regulator for the system. It acts as a fluid exhaust to the system and by controlling the flow rate of the water going through this valve, the pressure at the actuators can also be controlled. To actuate the fingers, fluid needs to be delivered from the water pump to the fluidic actuator. Each finger has a three way, two position solenoid valve controlling the flow of water into the finger. Five degrees of motion are achieved with five solenoid valves which are mounted on a block of manifold.

The three way, two position solenoid valve has three ports. Water from the pump is directed towards port 1. When the valve is switched on, water will flow into port 1 and out of port 2, into the fluidic actuators in the finger. The joints bend with increasing water pressure. Water inside the finger maintains its pressure with the valve switched on. When the valve is turned off again, water will lose its pressure. The restoring force in the joints will push the fluidic actuator back to its original form and the extra volume of water out of the finger. Water is returned back through port 2 and out of port 3, which is connected to the reservoir.

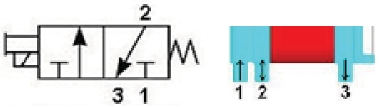

Figure 2. 3/2 solenoid valve ports and symbol.

Water is delivered to the inlet of the manifold and distributed into port 1 of each valve and to the pressure sensor, used to monitor the pressure of the water supplied into the fingers. Individual pipelines are laid out inside the manifold in order to connect the finger tubing to the common ports of each valve. Water coming out of port 3 is directed to a common pipeline inside the manifold, and comes out of the manifold outlet and into the reservoir.

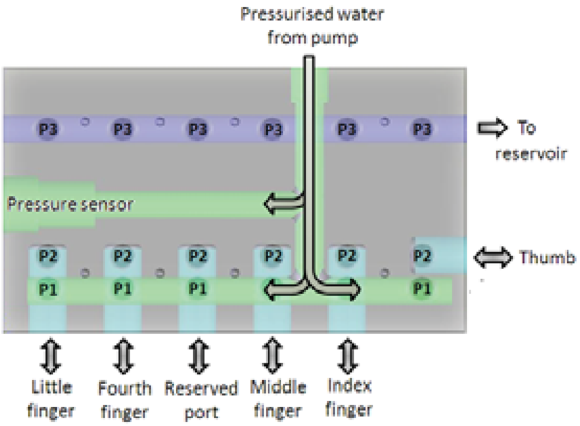

Figure 3. Internal flow diagram of manifold.

3. Finger Design

The proposed hand utilises an under-actuated approach, i.e. the actuators of the hand are less than the DOF of the hand, but the mechanical design of the hand allows the hand to perform automatic shape adaptation.

The proposed finger design consists of only one unit, i.e. the joint and phalange sections are not separated. They are made with urethane, a soft, bendable but strong polymer. This is to create an adaptive grasp and to simplify the fabrication process of the hand, while decreasing the cost and allowing for future mass production. Fluidic actuators are placed between the phalanges as finger joints. Figure 4 shows the general layout of the finger. The embedded fluidic actuator consists of a heat shrink tube, which expands as pressurised water pumps in, a spring, which constrains the heat shrink folds, elastic strings, which provide extra restoring force for the finger to return to its original position as pressure ceases, and epoxy, which is used as a sealant for the end of the tube (Figure 5).

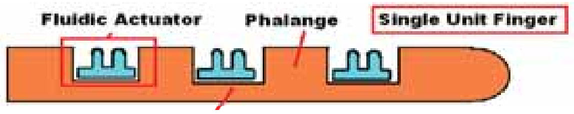

Figure 4. General layout of the proposed finger

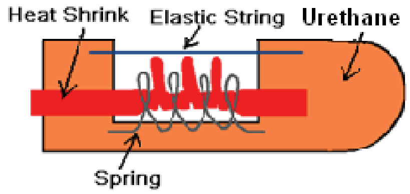

Figure 5. General layout of the joint

As each solenoid valve will allow one flow channel, it has been decided that there will be one channel per finger because this can minimise the space taken up by the solenoid valves, yet still maintain sufficient manoeuvrability. Each joint has one DOF due to the one flow channel; therefore each finger has three DOF, and the thumb has two DOF. Ideally the thumb should have three DOF but this will complicate the placing of the flow channels. Therefore the abduction/adduction movement of the thumb has been eliminated. This defect is improved upon by placing the thumb perpendicular to the palm and thus the thumb will always oppose the fingers. Although this is different from the placement of the human thumb, this arrangement allows pinching and gripping to be achieved. The fingers are similar to a human hand, i.e. parallel with each other. The hand therefore has a total of 14 DOF.

The sequence of finger joints bending coincides with the adaptive gripping concept. For each folding fluidic actuator to bend, water must flow through it. This means that for the second joint to bend, the first joint must first bend to allow water to pass through. Therefore, if the proximal phalange (the phalange that is closest to the palm) is in contact with an object, as the applied pressure increases, the extra force will not be used to bend the MP joint (the joint what is closest to the palm). This is because there is no space for this movement. Water will therefore pass through and bend the rest of the joints. This cascade design mimics human gripping, especially when a person is not certain about the size of the object.

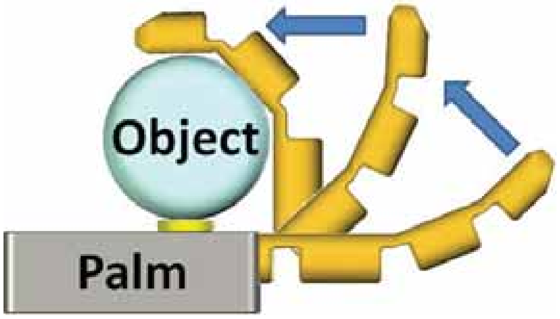

Figure 6. Gripping steps of the proposed finger

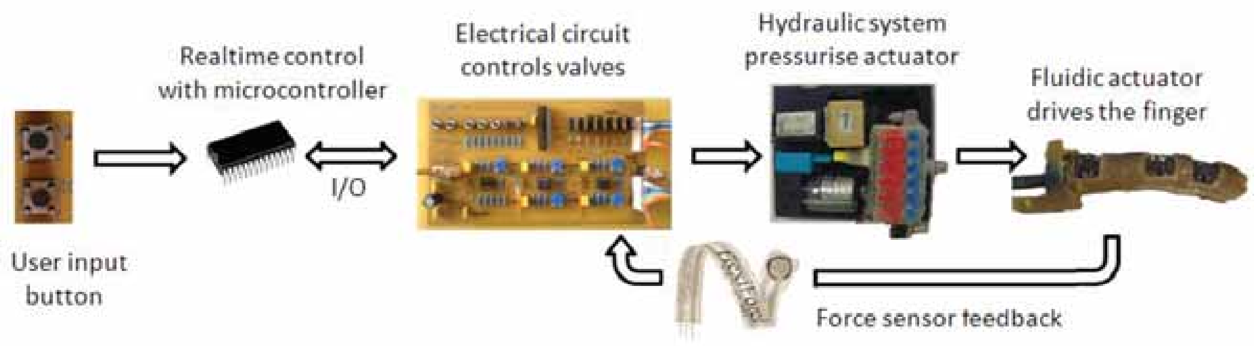

Figure 7. Overall control diagram of the system

4. Control System

The control system and electronic hardware consists of inputs from the force sensor, pressure sensor and user interface as shown in Figure 7. The input signals are processed through the micro-controller, and outputs to the pump, flow control valve and solenoid valves are determined based on the embedded program inside the controller. All the electrical circuitry is designed, fabricated and implemented onto a PCB.

The prosthetic hand is designed to be controlled by an embedded microcontroller to promote portability of the device. The roles of the microcontroller are: to take digital inputs from the push buttons of the user interface; to take analogue inputs from the force sensor and pressure sensors; to process these input signals and provide the digital control signal for the pump and the solenoid valves and to provide PWM signals for the flow control valve.

User Input

The user can select between operating the hand under manual mode or automatic mode. In the manual mode, the fingers and solenoid valve switching are controlled by five push buttons. In the automatic mode, the hand can grab onto objects automatically without push buttons. This is achieved through object detection with force sensors attached to the palm.

In the automatic mode, there are four states: relaxed, object detection, gripping and object removal. In the relaxed state, the solenoid valves are switched off and fingers are relaxed. Once an object is detected by the force sensor, the force sensor reading is recorded as an indication of object mass. The solenoid valves are switched on and pressure in the system is increased until the object is firmly gripped. The solenoid valves will turn off returning the fingers to the relaxed state when the object is removed.

Pressure Control

Pressure in the system is proportional to the flow rate of water through the flow control valve. The valve receives PWM signals from the microcontroller. Pressure can therefore be increased by increasing the duty cycle of the PWM signal.

Force Sensing and Control

Objects are detected by the force sensors attached to the palm. The sensors are based on piezoresistive material. The resistivity of the sensor will decrease as the force applied to sensor increases. Therefore, the mass of the object can be calibrated by monitoring the sensor readings. Force sensors are also attached to the fingertips in order to have force feedback for grip force control.

5. Experiments and Results

Experiments are conducted in order to determine the characteristics of the design and detect possible improvements for future work, speed, force, and position control. Some hand characteristics with respect to gripping motions are also presented below:

Speed of motion

The time required for the hand to bend fully is about four seconds with full pressure (5 bars), and eight seconds with 4 bars of pressure. However, this time is only an average value due to the slight difference between each finger. The finger with a thinner joint base will tend to bend faster.

Finger force

Two grasping motions, gripping and grasping, have been tested on the robotic hand to evaluate its strength. Objects with known weights are used for grasping and holding. These weights have been added until slipping occurs. The maximum force achieved by gripping motion is 0.70kg and the maximum force achieved by holding is 2.4kg. Higher gripping force is achieved with the use of latex gloves, which increases the maximum gripping force to 2.1 kg.

Adaptiveness

The hand has successfully gripped objects with different shapes and sizes (Figure 9). It is worth noting that the performance of adaptive grasping is close to a human finger as each finger wrap around the object according to the shape of the object.

Figure 8. Various activities performed by the hand

Figure 9. Various activities performed by the hand

6. Conclusions

A robotic hand that aimed to imitate a human hand, with regards to the size, appearance, and functions performed has been developed. The combination of the hydraulic actuating system and the fluidic actuators has proven to perform human finger bending motions by controlling the pressure applied to each finger. Intrinsic placement of the hydraulic parts allows the hand to be portable but still be able to supply sufficient strength. A controller is made to operate the hand and to realise the concept of it being a prosthetic hand.

Acknowledgements

Project supervisor – Dr Shane Xie
Lab technician – Ken Snow
Graduate student – Sean Manley

References

1. National Aeronautics and Space Administration. *Robonaut.* Retrieved March, 2008 from http://robonaut.jsc. nasa.gov/ sub/hands.asp
2. Haemmerle,E. (2007) Industrial Automation. Lecture handout, *Robotics.* University of Auckland.

Low cost bi-directional flow sensor using back-to-back Pitot tubes

Zhe Charles Lu, Andrew Lau
The University of Auckland,
Department of Mechanical Engineering,
Mechatronics Engineering,
New Zealand

Abstract

A low cost bi-directional air flow sensor was developed using back-to-back Pitot tube arrangement. By measuring the difference between ‘up’ and ‘downstream’ air pressures using a differential pressure sensor, it is possible to determine the fluid flow rate. The sensor was successfully calibrated to 70 L/min. It has a sensitivity of ±1 L/min, and an accuracy of ±10.4 % over a working temperature range of 0 – 50 °C. However in reality the accuracy is likely to be significantly higher. This flow sensing technique was proven to be reliable and consistent.

Keywords: *bi-directional, flow sensing, Pitot tubes, low cost, differential pressure sensor*

1. Introduction

During the development of a mechanical breathing simulator, an airflow sensor was needed for flow feedback control. Commercial flow sensors are expensive to buy. A fast response and accurate sensor can cost approximately US$1000. For research purposes, a sensitive, accurate and bi-directional low cost airflow sensor is required.

2. Background

Most flow sensors in the market today use the hotwire anemometer technique. By heating up a thin wire inside a flow stream, the rate of cooling can be used to determine the fluid velocity [1]. There are several disadvantages with this method. Firstly, only very clean flows can be measured, as any dirt that got trapped on the wire will result in an inaccurate reading. As a result the sensor must be recalibrated frequently. The hotwire is an extremely thin wire, often only a few microns thick, which makes it very fragile. The third disadvantage is that this technique is not bi-directional.

The use of Pitot-static tubes is another technique commonly used to measure fluid flow. By measuring the difference of the pressure parallel and perpendicular to the flow stream, the dynamic pressure of the fluid can be calculated using Equation 1. The fluid velocity can then be derived with Equation 2, if the head loss coefficient *K* and the fluid density *ρ* is known. However, this measurement technique also cannot measure in both directions.

$$P_{dynamic} = P_{stagnation} - P_{static} \qquad (1)$$

$$P_{dynamic} = K\frac{1}{2}\rho V^2 \qquad (2)$$

3. The Concept

In order to achieve bi-directionality, a back-to-back Pitot tube arrangement was proposed. By placing two Pitot tubes with their openings arranged to face the opposite directions, parallel to the flow stream, it becomes possible to measure bi-directional flow. Ignoring any suction effect, the side facing the flow would measure the stagnation pressure, while the other side would only measure the pure static pressure. Then this problem can be solved using a conventional Pitot-static tube analysis. Reversing the flow would then give a negative pressure difference, thus achieving bi-directionality.

To measure the pressure difference, a differential pressure sensor can be used. The 26PC series piezoresistive pressure sensor made by Honeywell is highly linear, sensitive and has a response rate of 1 kHz. The lowest pressure range available is 1 PSI, and was selected for use as the flow rate required to measure was very small.

However, there are several difficulties with the usage of this differential pressure sensor. As these differential pressure sensors are designed to measure liquid pressure, 1 PSI is still significantly larger than the required working range of the air flow sensor design. Therefore a sensor with higher precision and a smaller full scale range would be more suitable. In addition, the sensor only outputs ±16.7 mV at full scale, which means that the signal must be amplified before it can be used. Nevertheless, this sensor is still able to achieve the desired performance required.

Based on Equation 2, the relationship between the voltage output and the volume flow rate in a back-to-back Pitot tube arrangement can also assumed to be a quadratic relationship shown in Equation 3. Coefficient *C* is influenced by circuit amplification, flow pipe characteristics and fluid properties, and can be obtained through calibration.

$$Voltage = CV^2 \tag{3}$$

4. Circuit Design

The signal output from the pressure sensor needs to be amplified to ±10 V to be compatible with a digital to analogue converter, which means that the gain of the circuit has to be above 600. Variables such as sensor placement, and flow duct geometry can all affect the percentage of the full scale range achieved, thus the actual gain required.

A two stage amplification circuit was designed to achieve the gain needed for the sensor. The first stage consists of an instrumentation amplifier. It was chosen because this configuration has a very high input impedance and low noise, DC offset and drift, which should result in a more accurate sensor reading [2]. The second stage is an inverting amplifier with offset adjustment, used to eliminate any DC voltage offset after the first stage. A low pass filter with a cut-off frequency of 20 Hz was also added in order to minimise any high frequency noise present at the output. Both stages will share the required gain, which will be determined from experiments.

Since a high gain was expected from the circuit, NE5532 ultra low noise dual op-amps were used, as any noise at the input end will be amplified and interfere with the reading. Power supply bypassing capacitors were also added to the circuit to filter out high frequency noise, and to smooth the supply voltages.

To supply power to the op-amps and the sensor a dual polarity power supply circuit was designed. It features a centre-tapped step down transformer to provide the correct voltage range from the mains voltage. The voltage is then rectified, passed through a series of capacitors for filtering, and through two regulators in order to obtain the ±12 V needed by the components. The transformer’s centre-tap would then act as a virtual ground between the voltages.

The circuits were designed and fabricated onto printed circuit boards, as shown in Figure 1. This was done to further minimise noise as well as making the circuit more compact.

Figure 1. Printed circuit boards containing the power supply circuit (top) and the amplification circuit (bottom)

To protect electronics from the environment, it was decided to place them inside a self-contained box, shown in Figure 2. A mains fuse and a switch were mounted on the side of the box, along with a status LED. A fan was also mounted on top to cool the transformer and components.

Figure 2. Electronics jiffy box

All cables travelling between the differential pressure sensor and the circuit board are shielded to prevent from acting as an antenna and picking up mains hum from the surroundings.

5. Flow Pipe Design

The flow pipe design is critical to the performance of the flow sensor. Variables such as material, Pitot tube placement, pipe dimensions and geometry can all play a role in the quality of the readings received by the differential pressure sensor.

The two Pitot tubes would be placed carefully at the centre of the flow pipe cross-section, as the stream velocity is always highest at the centre point of the flow stream [3]. The Pitot tubes were also placed as close as possible in order to minimise the difference in static pressures (Figure 3).

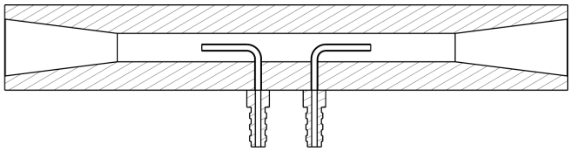

Figure 3. Cross-sectional view of the flow pipe and the Pitot tube placement

The inner diameter of the flow pipe controls the flow velocity. The smaller the pipe diameter, the higher the flow velocity, and the higher the dynamic pressure experienced by the sensor. This increases the accuracy of the readings, as a higher percentage of the full scale range can be utilised. Also, less gain is needed by the amplification circuit, making it more stable. However, a smaller tube diameter will also place more restriction on the flow. Therefore, a balance between the flow velocity and pipe restriction must be achieved.

By using ANSYS CFD analysis, it was determined that a 6 mm pipe diameter would give approximately 50 per cent of full scale range at the required flow rate of 70 L/min.

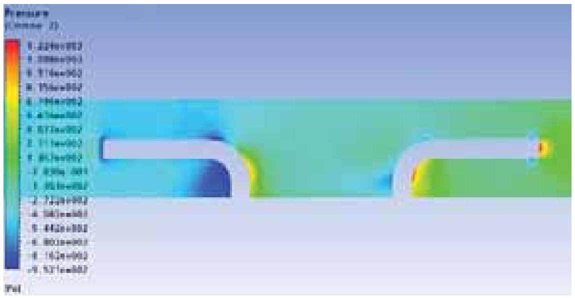

Figure 4. ANSYS flow sensor analysis (pressure)

Upon closer examination of the analysis, the back-to-back Pitot tube arrangement appeared to give an unexpected added benefit. The downstream Pitot port experiences a large suction pressure. The blue region in Figure 4 illustrates that the pressure is significantly lower at the downstream opening of the Pitot tube. At a flow rate of 70 L/min, the CFD analysis produced a result of 1200 Pa at the upstream opening compared to -875 Pa at the downstream opening. This suction effect increases reading significantly, which means that the amplification gain can be made lower, and the sensor's accuracy would also increase due to higher utilisation of the 1 PSI full scale range.

The flow pipe was fabricated using Acetal plastic. A piece of locking plate was also made from the same material to secure the Pitot tubes to the flow pipe, by wedging in between the barbed ports and the pipe. The completed assembly is shown in Figure 5.

Figure 5. Flow sensor assembly

6. Testing and Calibration

The flow sensor assembly was calibrated against a RespiCal Timeter Calibration Analyser, which has an accuracy of ±2 per cent reading. The calibration setup is illustrated in Figure 6.

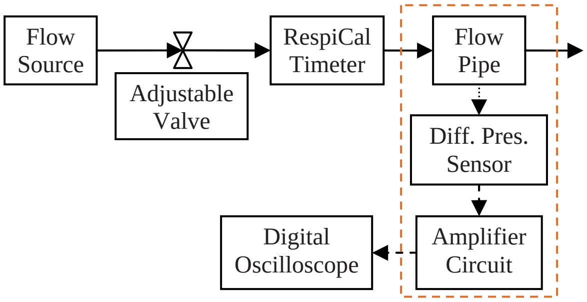

Figure 6. Flow sensor calibration equipment setup

The actual gain of the circuit was set to 900, and the raw data of the calibration can be seen in Figure 7. The relationship between voltage and flow rate does appear to be quadratic as expected.

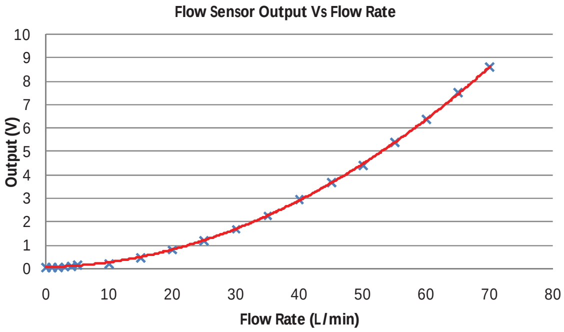

Figure 7. Calibration result for the forward direction

To determine the coefficient *C* as described in Equation 3, least squares method was applied with the help of MATLAB to trend the data. It was found that both forward and the reverse direction obtained good fit and similar coefficients, which means that the back-to-back Pitot tube configuration gives stable results. Therefore, *C* for the forward and the reverse direction was determined to be 23.68 and 23.76 respectively. Figure 8 shows the comparison between the raw data and the fitted curve in the forward direction.

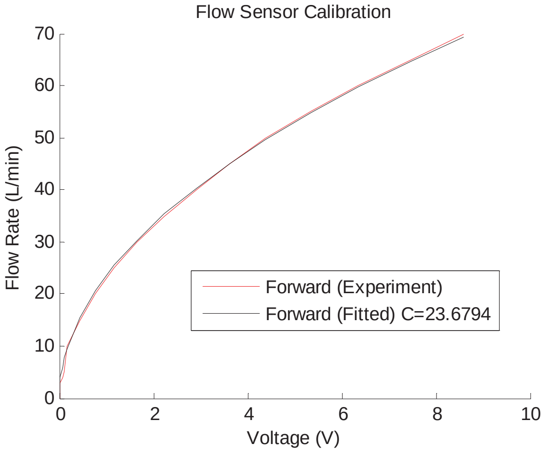

Figure 8. MATLAB least squares fit of flow sensor calibration data for the forward direction

While the quadratic curve generally fitted the data very well, it can be seen that at lower flow rates (Figure 9), this is not the case. There are several plausible explanations. Firstly, due to the quadratic relationship between output voltage and flow rate, when the flow halves, the pressure sensed falls by four times. Therefore, at lower flow rates, the sensor would loose accuracy due to the sensitivity of the pressure sensor as well as noise and instability in the amplification circuit. Another possibility is that at lower flow rates, the flow inside the flow pipe becomes laminar, which changes the flow profile, and the coefficient determined is no longer correct. The actual cause of this is most likely the combination of the two.

The sensor can be used in a wide temperature range of 0 – 50 °C, which is the operating temperature range for the pressure sensor. While the differential pressure sensor is temperature compensated, the air density changes by up to 8.4 per cent throughout the sensor's operating temperature range. This will have an effect on the pressure applied to the Pitot tubes, and is the limiting factor of the flow sensor's accuracy. Thus, the accuracy of the flow sensor was determined to be ±10.4 per cent over the full working temperature range. However under normal working conditions, the temperature usually remains constant, so the accuracy is likely to be much higher.

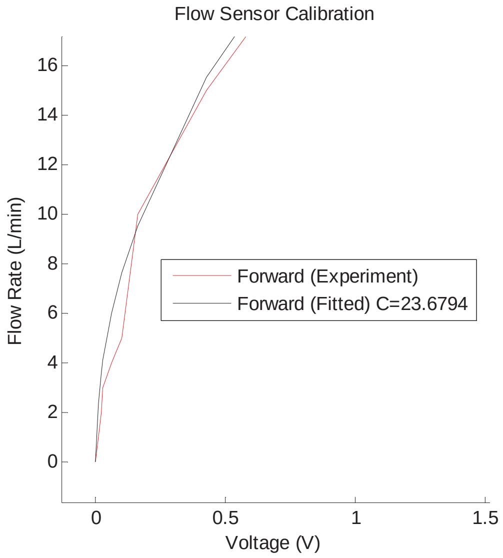

Figure 9. Detailed view of the flow sensor calibration data fit for the forward direction

When the flow sensor is idle, the noise in the electronics produces around ±1 L/min of noise. This is not a problem as it is very small compared to the calibrated full scale.

7. Conclusions

The flow sensor utilising a back-to-back Pitot tube design has an accuracy of ±10.4 per cent over a working temperature range of 0 – 50 °C with a sensitivity of ±1 L/min. Under normal operating conditions, the accuracy is likely to be significantly higher.

The bi-directional flow sensor has an analogue voltage output between ±10 V, with a response rate of 1 kHz, and was calibrated up to 70 L/min. It can be demonstrated that this back-to-back Pitot tube arrangement works reliably and consistently. The flow sensor cost less than NZ$100 therefore it is a very low cost alternative with very good performance.

Acknowledgements

The authors wish to thank Dr. Roger Halkyard for supervising the project, Dr. Kean Aw for advice on circuit design, and Fisher & Paykel Healthcare Ltd. for providing access to the workshop.

References

1. McKetta, J.J., Encyclopedia of Chemical Processing and Design. Vol. 22. 1985, New York: Marcel Dekker Inc.
2. Jung, W., Op Amp Applications Handbook. 2005: Elsevier-Newnes.
3. Cengel, Y.A. and R.H. Turner, Fundamentals of Thermal-Fluid Sciences. 2nd ed. 2005, New York: McGraw-Hill.

The UoA Undergraduate Mechatronics Research Journal , Vol. 1

Hardware Integration of a Mobile Two-Wheel Balancing Platform for Autonomous Applications

Vivien Coelho, Stanley Liew
Department of Mechanical Engineering
The University of Auckland ,New Zealand

Abstract

This paper discusses the hardware integration of a mobile two-wheel balancing platform for trajectory control and testing of autonomous mobile applications. Two-wheeled platforms have the advantages of being agile and are inherently dynamically stable with a smaller footprint. Two controllers, a reference tracking controller for speed and a PId controller for turn rate were designed for trajectory control. Wheel encoders, an IMU and a gyroscope are used to measure the speed, turn rate, tilt angle and tilt rate of the platform. This sensor data and control algorithms are processed on an embedded PC, the Athena which used MATLAB and Simulink. A second embedded PC, the Mini-ITX is responsible for implementing sophisticated autonomous applications such as obstacle avoidance using 'Player', a well known robot software interface. In the future, obtaining less noisy speed and turn rate state information of the platform will further improve controller performance.

Keywords: *Mechatronics, balancing platform, two-wheel.*

1. Introduction

The prevalent use of robots will be the norm of the day in the very near future. Current technology indicates considerable potential for the use of autonomous robots for military applications, and as service robots in households and industries such as entertainment, construction and healthcare [1]. Specific applications would include tour guides in museums, mobile blood-pressure and sugar level testing units in hospitals, and lawn mowing/vacuum cleaning robots for households.

Mobility is a vital aspect of the autonomous robots described above. Two-wheel robotic platforms lend themselves to these applications. They are derived from a well known classic control problem, the inverted pendulum.

Recently, extensive research has been conducted in the area of two-wheel balancing platforms. Segway Inc. has released the Segway RMP range [2] for a wide range of indoor and rugged outdoor applications. The Segway RMP 200 is designed for research in autonomous applications and can carry a maximum payload weight of 91kg. Research projects include the CIIPS Platform, which employs a gyroscope to measure tilt rate, an inclinometer to measure tilt angle and wheel encoders to measure the speed of the platform [3]. Its main purpose is to compare the performance of a linear-quadratic regulator (LQR) controller with a pole-placement controller for balancing. A LQR controller observes the states of the platform and the control effort to find an optimal solution. A pole-placement controller arbitrarily places poles in order to determine the control effort required. Both types of linear controllers were able to balance the platform but the LQR controller was found to be more robust than the pole-placement controller. A PID controller was implemented for trajectory control with reasonable success. The second research platform evaluated, the Fuzzy Controller Platform, uses the same basic type of sensors as the CIIPS platform. However it implements a fuzzy controller for motion control of the platform [4]. Fuzzy controllers do not require an accurate mathematical model of the system dynamics and in those respects are easier to implement. Fuzzy controllers also have the ability to adjust to changes in system dynamics and provide more stable control. Both the CIIPS Platform and the Fuzzy Controller platform are built on a small scale, primarily for testing controller performance.

JOE is an example of a research platform built on a larger scale. JOE was among the first two-wheel balancing platforms to be built and tested [5]. It is capable of speeds up to 1.5ms^{-1}. Hardware was carefully considered in order to minimize backlash and develop a robust and stable platform. Two decoupled state space controllers were implemented for trajectory control. JOE uses wheel encoders for sensing the speed of the platform and a gyroscope to obtain the tilt angle and tilt rate.

Although a lot of research has been conducted into the stabilisation of two-wheel balancing platforms over the past decade, there has not been significant work carried out into alternative actuation methods. Last year research was conducted into alternative actuation methods for two wheeled balancing platforms [6]. The addition of a reaction wheel actuator was investigated to reduce energy consumption while balancing. Experimentation showed that the reaction wheel actuator consumed approximately 21% less energy than balancing the platform with only the main drive wheels. However further mobility of the platform was not investigated.

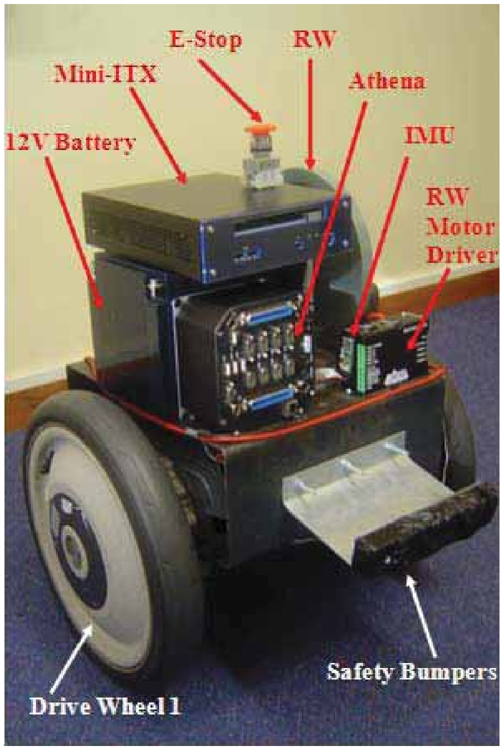

Figure 1. Photograph of Platform

In this paper, the hardware required for mobility of the platform for indoor use is investigated. This provides an alternative product to the Segway RMP 200. The main focus is to enable easy and convenient testing of autonomous applications such as obstacle avoidance and people following.

2. Problem Formulation

The aim of this project is to develop a mobile two-wheel balancing platform for further research into autonomous applications. Specific tasks include:

1. Development of controllers for the mobility of the platform.
2. Integration of hardware for data acquisition and balancing of a mobile platform.
3. Integration of basic sensors to measure the state of the platform for trajectory control.
4. Implementation of hardware to enable execution of sophisticated autonomous applications.

3. Controllers

Two independent controllers have been developed to control the motion of the platform – a reference tracking controller to control the forward speed and a PID controller to control the turn rate. It is assumed that the longitudinal and lateral motion of the platform is decoupled. This is reasonable at small angles. The controllers are further discussed below.

Balance and Speed Controller

A linear state-space controller was used to balance and maintain the speeds of the platform. The same approach can be seen in [7]. State variables chosen are:

$$\underline{x} = \left[\theta \quad \dot{\theta} \quad v \quad \int\left(v_{ref} - v\right)dt\right]^{T} \tag{1}$$

$$T_{BSC} = -K\underline{x} \tag{2}$$

where $\underline{x}$ is the state vector, θ is the tilt angle, $\dot{\theta}$ is the tilt rate, and v_{ref} is the reference platform speed. The last state variable provides the necessary reference tracking to the desired speed.

The gain matrix *K* in the full-state feedback control law (2) is calculated as a linear quadratic regulator (LQR).

Turn Rate Controller

A proportional-integral-derivative (PID) controller (3) was developed to control the turn rate of the platform.

$$T_{TRC} = K_P e(t) + K_I \int_0^t e(t)dt + K_D \frac{de(t)}{dt} \tag{3}$$

where T_{TRC} is the commanded wheel torque difference, K_P, K_I, K_D are the controller gains and *e(t)* is the turn rate error ($\dot{\gamma}_{ref} - \dot{\gamma}$).

Tuning with both controllers simultaneously was initially done in simulation, prior to implementation on the physical system.

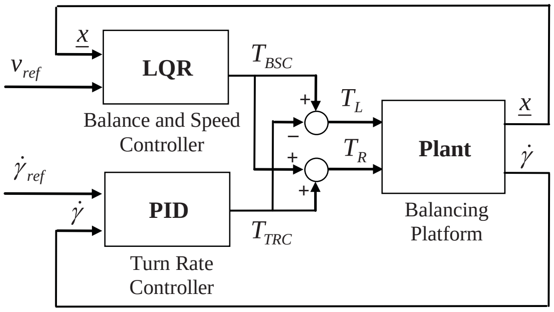

Figure 2. Block diagram of the control system

4. System Overview

The controllers designed require information concerning the speed, tilt angle, tilt rate and turn rate of the platform. These sensors required onboard data acquisition before feedback to the controllers. Additional hardware for data acquisition is also required.

Keeping these considerations in mind, a layout of the system was planned as shown in Figure 3. An embedded PC, the Athena from Diamond systems is responsible for controlling the trajectory of the robotic platform given a desired speed and turn rate. It processes the information from the principal sensors – the wheel encoders, the Inertial Measurement Unit (IMU) and the gyroscope, and outputs a desired current to the actuators, two brushless DC motors. The desired current is processed by the B40A8 servo amplifiers which outputs power to the motors.

The wheel encoders are hall sensors integrated with the brushless DC motors from the original Segway. They measure the instantaneous speed and turn rate of the platform. The IMU measures the tilt angle (angle relative to ground) of the platform and sends the information over RS232. The gyroscope returns the tilt rate. The wheel encoders via the servo amplifiers and the gyroscope use the analog to digital data acquisition capabilities of the Athena.

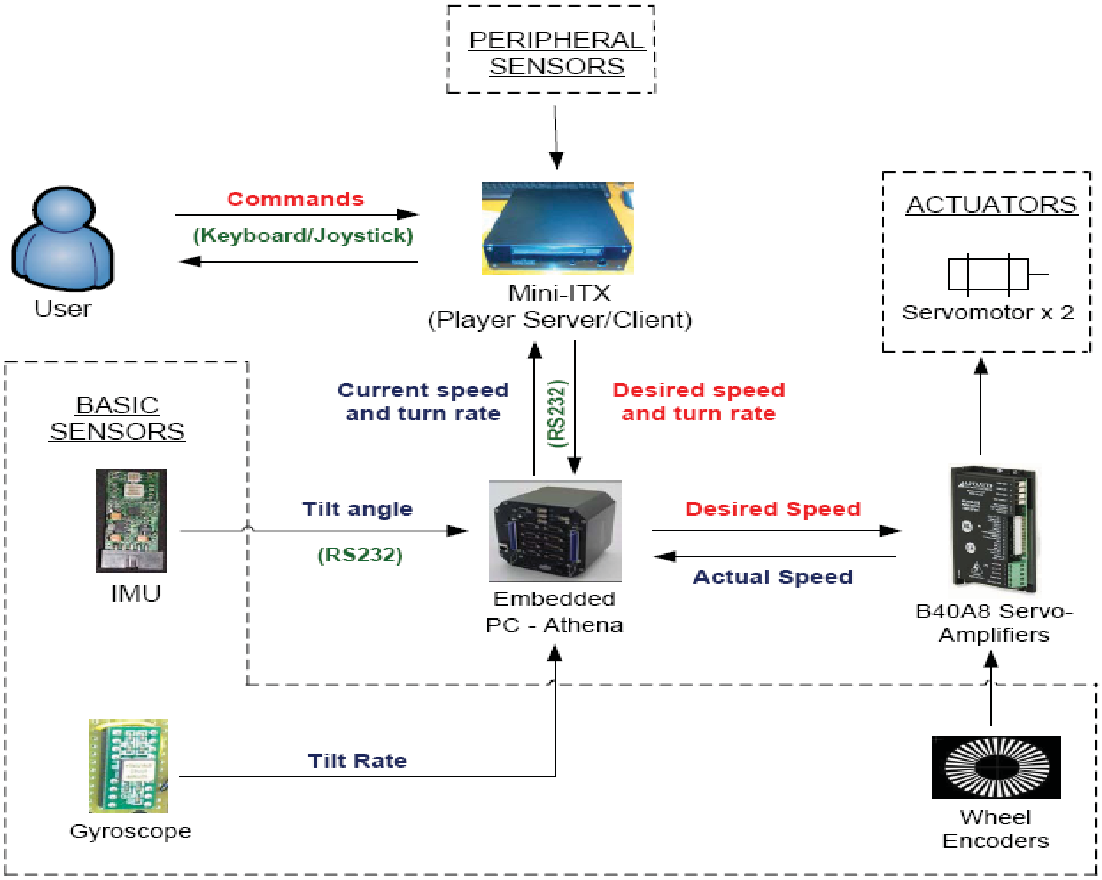

Figure 3. System Overview

The Athena also executes the algorithms of the controllers discussed above. These controllers are implemented in Simulink on a desktop PC. Simulink uses Real Time Workshop and xPC Target to create an executable that is downloaded and run on the Athena.

The desired speed and turn rate for the platform is sent to the Athena from the Mini ITX (VIA Technologies) over a RS232 connection. The Mini ITX is responsible for higher level control such as planning the trajectory of the platform (path planning). The operating system used is Linux. A hard disk and a compact flash card both have the necessary software installed on them. The hard disk is used for testing, independent of the platform. The compact flash card is used when executing programs on the platform.

Player, an open source programming software that allows robot control programs is used on the Mini ITX [8]. It provides a way to communicate information between the platform and the peripheral sensors. Programs have been written and executed within Player that read in information from a peripheral sensor, calculate a desired speed and turn rate and send this information to the platform via RS232, to determine the desired speed and turn rate for the platform. Alternatively, the user can directly control the desired speed and turn rate of the platform via a keyboard or joystick.

5. Sensor Performance

Wheel Encoders

Data from the wheel encoders is used to calculate the speed and turn rate of the platform. The wheel encoder signals displayed some significant amount of noise present in the signals. The signal to noise ratio for wheel encoder 1 was calculated to be 23dB. This low value indicates a strong presence of noise in the signal when compared to the presence of the actual signal. This noise affects the measured states of the system and provides inaccurate information to the controllers. Smoother, more accurate data would ensure that the controllers do not attempt to correct nonexistent errors in the state of the platform.

In an attempt to remove noise, two types of filters were tested with different cut-off frequencies – a simple low pass filter and two low pass filters in series. Figure 4 shows data filtered by two low pass filters in series with cut-off frequencies of 2.5Hz. The filtered data is very smooth but exhibits a delay of approximately 1s. A delay this large would give delayed information regarding the state of the platform to the point where balancing is no longer achievable. It was decided that filters would be chosen to have a maximum delay of 0.1s regardless of the smoothness of the filtered data. A single low pass filter was applied to the speed information. The filter attenuates signals with frequencies over 15Hz in an attempt to remove the noise in the wheel encoder readings. The filter smoothes the data and exhibits an acceptable delay of approximately 0.1s.

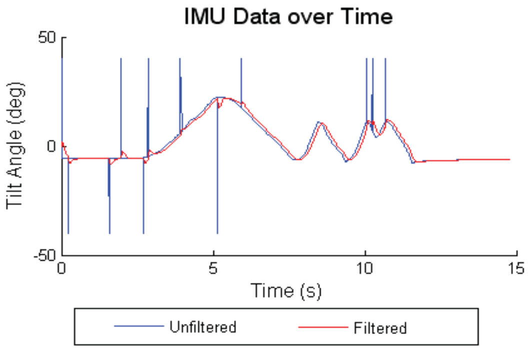

Figure 5. IMU Data over Time

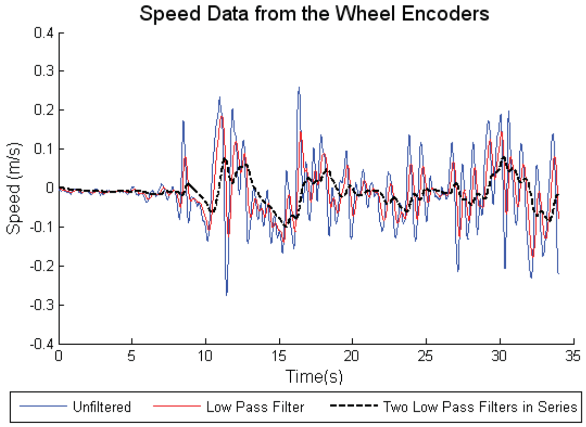

Figure 4. Speed Data from the Wheel Encoders

IMU

Data from the IMU is used to calculate the angle of the platform. The signal from the IMU was also investigated. It exhibited some spikes that occur for a brief instance in time. This is non-ideal as it could cause the controller to exert very high, unnecessary effort onto the motors. To remove these spikes, two low pass filters was also implemented in series to ensure robust sensor readings. Figure 5 shows a graph of the IMU output before and after filtering.

Each filter in turn attenuates frequencies of over 20 Hz. Using a single filter requires attenuation at higher frequencies which also attenuates the measured signal. The filter smoothes the data successfully and exhibits an acceptable delay of approximately 0.1s.

Gyroscope

Data from the gyroscope is used to calculate the tilt rate. There was some evidence of noise in the signal. However it is less noisy than the data from the encoders and IMU. A single low pass filter was applied to the signal. The filter attenuates signals with frequencies over 15Hz. The filter exhibits an acceptable delay of approximately 0.1s.

6. Setting up an Autonomous Application

Work was continued in setting up the software required for autonomous applications. One of the autonomous applications that can be executed on the platform is a simple obstacle avoidance algorithm found in the Player example files.

This algorithm requires the use of a laser scanner to detect the obstacles present in the environment. The algorithm then calculates a desired speed and turn rate for the platform to avoid the obstacles. The Hokuyo UBG-04LX-F01, a scanning laser range finder was implemented as the peripheral sensor. Figure 6 shows the output of the laser scanner through Player.

7. Discussion and Conclusion

A mobile two wheel balancing platform has been developed. A linear state-space controller for balance and speed reference tracking has been designed in conjunction with a PID controller for turning. Two embedded PCs were implemented – the Athena for data acquisition and execution of control algorithms and the Mini-ITX to manage higher level path planning of the robot. The Athena processes information from the wheel encoders measuring speed and turn rate, from an IMU measuring the tilt angle, and a gyroscope measuring the tilt rate of the platform.

The installation of Linux and the use of the Player Project program on the Mini-ITX have enabled easy implementation and testing of future autonomous applications.

The wheel encoders were found to be noisy which affected performance of the platform. The source of the noise needs to be investigated or these sensors replaced.

Acknowledgments

Special thanks to the technicians at the University of Auckland for all their help, especially Rob Earl, Barry Fullerton and Sunita Bhide. Thanks also to Keith Colson from RoboNZ for providing the Inertial Measurement Unit and Chris Chambers for his assistance with Player. Finally, many thanks to Dr. Karl Stol and Dr. G. Liu for their supervision.

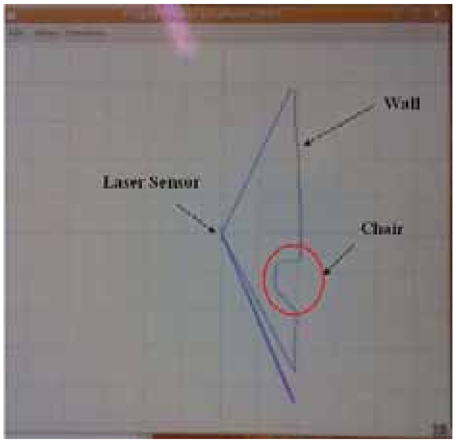

Figure 6. Output from UBG-04LX-F01 Using Player

References

1. Bekey, G. A. (2005) *Autonomous Robots: From Biological Inspiration to Implementation and Control*. MIT Press, Cambridge, MA.
2. “Robotic Mobility Platform (RMP)” (2008). Retrieved June 30, 2008, from http://www.segway.com/business/products-solutions/robotic-mobility-platform.php
3. Ooi, R. C, (2003) “Balancing a Two Wheel Autonomous Robot” University of Western Australia, Perth.
4. Chiu, C. and Peng, Y. (2006) “Design and implement of the self-dynamic controller for two-wheel transporter”2006 IEEE Conference on Fuzzy Systems, 480 – 483.
5. Grasser, F., Arrigo, A., and Colombi, S. (2002) “JOE: A mobile Inverted Pendulum”, IEEE Transactions on Industrial Electronics, **49**, 107-114.
6. Kalra, S., Patel, D, and Stol, K. (2007) “Design and Hybrid Control of a Two Wheeled Robotic Platform”, Proc. Australasian Conference on Robotics and Automation, Brisbane, Australia, 10-12 December.
7. V. Coelho, S. Liew, K. Stol, G. Liu (2008) “Development of a Mobile Two-Wheel Balancing Platform for Autonomous Applications,” 15th International Conference on Mechatronics and Machine Vision in Practice, Auckland, New Zealand, 2-4 December.
8. “Player” (2006) Retrieved on August 31, 2008 from http://playerstage.sourceforge.net/index.php?src=player

The UoA Undergraduate Mechatronics Research Journal, Vol. 1

Development of Rotary Joint Sensor using Ionic Polymer Metallic Composites (IPMC)

Jian Chew, Aidan van den Hurk
The University of Auckland,
Department of Mechanical Engineering,
Mechatronics Engineering,
New Zealand

Abstract

Ionic Polymer Metallic Composite (IPMC) is a type of smart material that has been proposed for use as a rotary joint sensor. Previous studies have identified the sensing properties of IPMC that would be useful for this purpose, but the testing methods are still inadequate, and more work needs to be carried out so that IPMC sensors can be used in measuring rotary motion.
A testing apparatus was constructed based on the mechanics of a human finger, and tested over a range of joint motions. The joint motion was defined in terms of the bending angle and bending rate and the effects of these components on the sensors response was investigated. Based on the results of the experiments, key relationships were identified between the bending angle and bending rate, and the peak voltage of the sensors response.

Keywords: *IPMC, Rotary joint sensing, smart materials*

1. Introduction

In recent years, the main barrier to advancements in sensors and actuators has been the limitations on materials used to create them. Problems often arise in applications where there are large numbers of mechanical joints located in close proximity, and insufficient room to place the required components. The development of “smart materials” such as Electro-Active Polymers (EAP) has shown potential to overcome this problem. EAP are polymeric materials that respond when an electrical stimulation is applied to it [1]. They can be divided into two categories; ionic and electronic, based on their activation mechanism [1,2]. Their behavioural properties have to be well understood and modelled if they are to be utilised as sensors and actuators in practical engineering applications.

Ionic Polymer Metallic Composites (IPMCs) are a type of EAP. They show properties similar to that found in a piezoelectric material; application of a mechanical deformation causes it to create an electrical voltage potential. The reverse effect is also observed. It uses the mobility or diffusion of ions to create this piezoelectric effect [1,2,3,4,5]. It has superior characteristics to conventional piezoelectric sensor materials such as zinc oxide, crystals and ceramics because it is mechanically flexible and is a natural bending element. Thus, they can be employed in applications that require sensing of a rotating mechanical joint [6,7,8]. IPMCs can also operate in wet conditions and do not require an external power source or auxiliary mechanisms, thus the complexity is significantly reduced [2,3,4,5,6,7,8].

Majority of research conducted on the practical applications of IPMC materials was in the field of actuation such as artificial muscles [7,9]. However, most of the research regarding their sensing abilities was focused on their feasibility to be used as a sensor due to its electromechanical properties, with limited research carried out on utilising them in practical applications.

For this project, the focus was on developing a model to describe the sensing behavioural characteristic of a Nafion based IPMCs for use in a practical biomechatronics application; as a rotary joint sensor to measure finger joint movement. Currently, data gloves are one of the only types of instruments that can accurately measure the kinematics of the finger joints. They are used in medical rehabilitation, sports science and virtual reality. However, they are expensive, usually costing more than NZ$15000 per pair because of the type of sensing material used; fibre optic cables [10]. Thus, new data gloves developed must have a sensing material that is cheaper, and the desired electromechanical properties to be applied for this application; flexible, lightweight, compact, quiet, ease of manufacture, formability, low power consumption and durable. IPMCs are a material that exhibits all of these desired properties.

2. Specification of IPMC strips

The IPMC material used in this analysis was sourced from Environmental Robots Inc., New Mexico, USA. Prior research has established the general sensing characteristics of IPMCs, but there is significant variation between specific sensors. Two IPMC strips of 0.4 mm in thickness, 22 mm in length and 8 mm in width were used in this research. Both strips have a distinct curvature, which was most likely caused by a combination of their former use, and dehydration. Throughout the duration of this research, the sensors were kept dry through exposure to room environment. Figure 1 shows an image of one of the IPMC strips used in this research.

Figure 1. IPMC strip used in this project. A NZ$1 coin is used for size comparisons.

3. Design and Construction of Controlled Testing Environment

The purpose of developing a testing environment is to provide a means for manipulating the IPMC sensor in a way that replicates the mechanics of a finger joint, and to provide a reliable method for acquiring meaningful data from the sensors output. It consists of three main components; mechanical, electrical and software as shown in Figure 2.

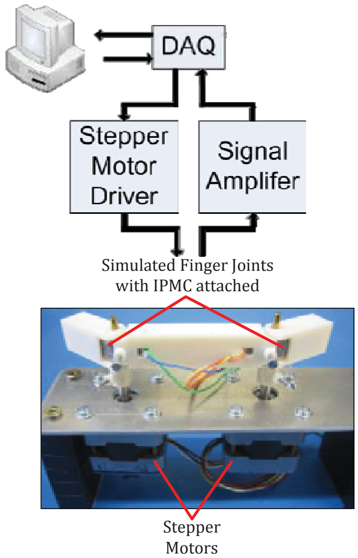

Figure 2. Controlled testing environment

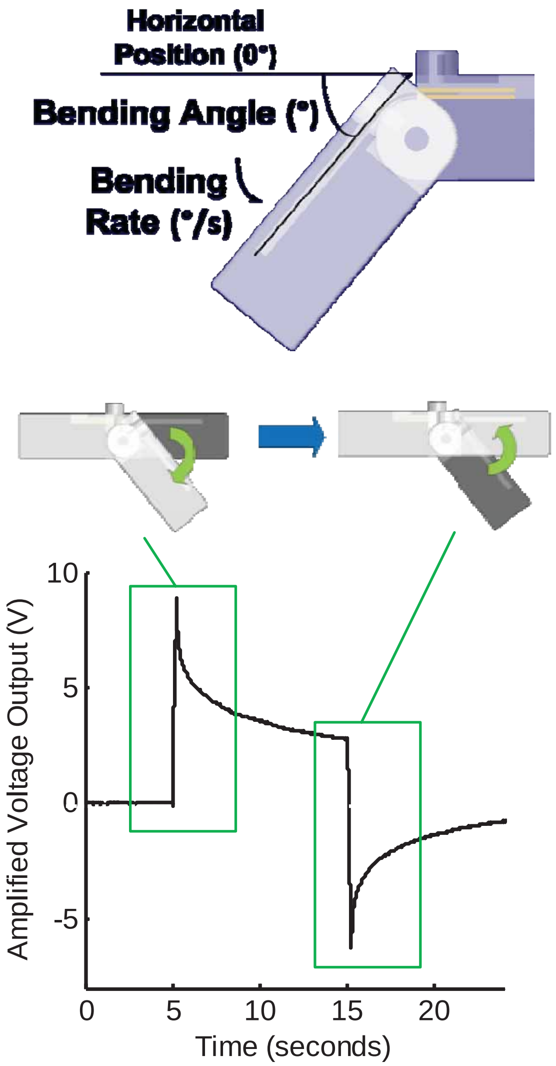

Figure 3. Definition of variables discussed and voltage response of IPMC due to joint motion

Figure 3 shows the variables that are discussed in this research together with an amplified voltage response curve of IPMC due to joint motion. As it can be noticed, the polarity of the change in voltages is dependent on the direction of bending.

Relating Peak Time, Bending Angle, and Bending Rate

The assumption that is used in this research is that the peak time (t_{peak}) that is extracted from the sensor response is equal to the actual time that the joint was in motion. Based on this assumption it is possible to form a relationship between the bending angle and the bending rate.

The bending angle (*D*) is the difference between the start and finish position of the joint, measured in degrees. The bending rate (*R*) is measured in degrees per second, and represents the angular velocity of the joint motion. This research does not explore the effects of acceleration, so the bending rate remains constant throughout the joint motion. Because the bending rate is always constant due to the use of stepper motor moving the finger joint, equation 1 can be used to relate the variables for a given motion.

$$R = \frac{D}{t_{peak}} \qquad (1)$$

The peak time can be extracted from the sensor response of a joint motion. The relationship shown in Equation 1 means that if either the *R* or *D* is known, the other can be found. This relationship also allows for the sensor response to be plotted against the joint angle, by multiplying all of the time values by *R*.

$$BendingAngle = Steps \times 1.8° \qquad (2)$$

$$BendingRate = \frac{1.8°}{t_{peak}} \qquad (3)$$

4. Experiment Method

The experiment procedure was designed to analyse the effects of the bending rate and ending angle on the sensor response. These effects were tested and analysed separately to determine how each component contributed to the overall response of the IPMC.

Bending Angle Response

The effect of the bending angle was analysed by conducting a series of experiments over a range of bending angles, at a constant bending rate of 450°/s. The results of these experiments are compared in Figure 4.

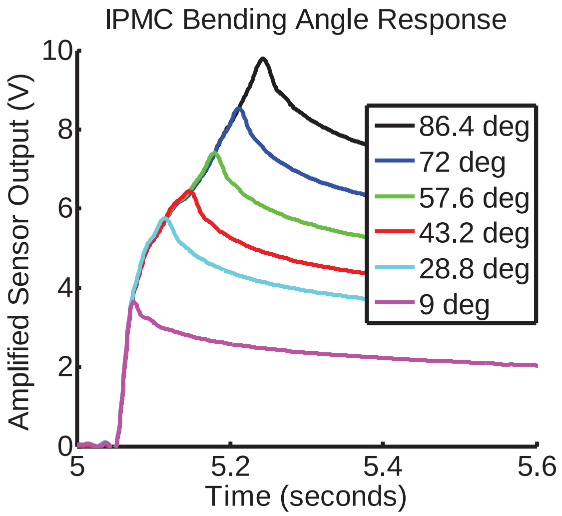

Figure 4. IPMC bending angle response

The most important trend in Figure 4 is that the sensor's output at every bending rate follows the same path up to the point where it reaches peak voltage. Previous research in this area has approximated this as a linear relationship, but the results show that this is not the case. This relationship means that the peak voltage for a motion to any angle can be determined based on the sensors voltage response to a motion to a larger angle.

Bending Rate Response

The effect of the bending rate was analysed by conducting a series of experiments over a range of bending rates, with a constant bending angle of 86.4°. The results of these experiments are compared in Figure 5.

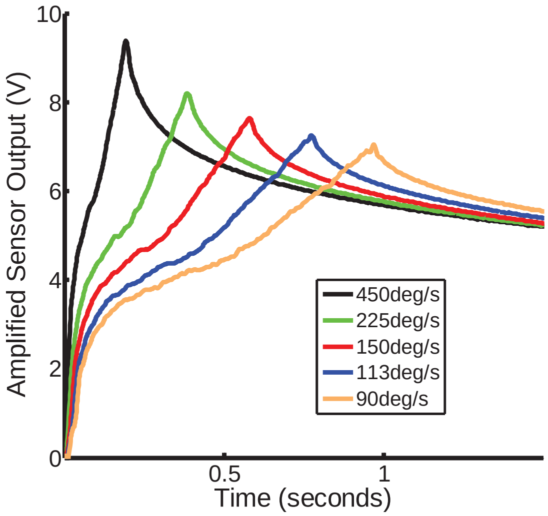

Figure 5. IPMC bending rate response

The experiment results highlight a number of interesting features in the IPMC sensor's voltage response. One of the important observations is that although the response is steeper for faster bending rates, the general shape is the same throughout all of the experiments. The other interesting feature is that the peak voltage decreases as the bending rate decreases. The physical explanation for this trend is that voltage recovery is occurring throughout the bending motion; so since a motion at a slower rate takes more time, a greater amount of voltage recovery occurs. A relationship between the sensors response to different bending rates can be based on the relationship between the peak voltages.

5. Conclusions

i. A test jig that mimics the movements of a human finger joint has been constructed for use in experiments.

ii. IPMCs have displayed behavioural characteristics that show potential for its use as a rotary joint sensor.

iii. The IPMC response at different bending angles follows the same path, up to the point where it reaches peak voltage.

iv. The IPMC peak voltage is lower for slower bending rates.

v. The relationships that have been observed in the bending angle and bending rate experiments could be used to create a model of the IPMC's response to bending.

Acknowledgements

We would like to acknowledge Mr George Blanchard for advice regarding digital filtering techniques, the technical support staff from the Department of Mechanical Engineering at the University of Auckland and the Mechatronics Engineering group, especially the class of 2008 for the unlimited support and generosity.

References

1. Carpi, F and De Ross, D (2005) "Electroactive Polymer Based Devices for E-Textiles in Biomedicine" IEEE Transactions on Information Technology in Biomedicine, **9**, 295.
2. Bar-Cohen, Y., Bao, X., Sheritt, S., and Lih, S.S (2002) "Characterization of the Electromechanical Properties of Ionomeric Polymer-Metal Composites", Proceedings of SPIE Smart Structures and Materials Symposium, EAPAD Conference, Paper 4695-33, San Diego, CA.
3. Shahinpoor, M., and Kim, K.J (2001) "Ionic Polymer-Metal Composites: I. Fundamentals" Smart Materials and Structures, **10**, 819 – 833.
4. Farinholt, K.M (2005) "Modelling and Characterization of Ionic Polymer Transducers for Sensing and Actuation" PhD Thesis, Virginia Polytechnic Institute and State University.
5. Bonomo, C., Del Negro, C., Fortuna, L., and Graziani, S. (2003) "Characterization of IPMC Strip Sensorial Properties: Preliminary Results" Circuits and Systems, 2003. ISCAS'03. Proceedings of the 2003 International Symposium on Circuits and Systems.
6. Shahinpoor, M., and Kim, K.J (2004) "Ionic Polymer-Metal Composites: III. Modelling and Simulation as Biomimetic Sensors, Actuators, Transducers, and Artificial Muscles" Smart Materials and Structures, **13**, 1362 – 1388.
7. Shahinpoor, M., and Kim, K.J (2005) "Ionic Polymer-Metal Composites: IV. Industrial and Medical Applications", Smart Materials and Structures, **14**, 197 – 214.
8. Biddiss, E. and Chau, T. (2005) "Electroactive Polymeric Sensors in Hand Prostheses: Bending Response of an Ionic Polymer Metal Composite", Medical Engineering & Physics , **28**, 568 – 578.
9. WorldWide ElectroActive Polymers Newsletter (2001), Vol 3, No. 2
10. Data Gloves by 5DT, Hand and Facial Motion Capture, Meta Motion. Retrieved April 20, 2008 from http://www.metamotion.com/hardware/motion-capture-hardware-gloves-Datagloves.htm

REVIEW ARTICLE

Characterisation and Bending Model of A Fully Hydrated IPMC Actuator

Thomas J Hurst
The University of Auckland,
Department of Mechanical Engineering,
Mechatronics Engineering,
New Zealand

Abstract:
An Ionic Polymer Metal Composite is a soft Electroactive Polymer material capable of high speed, high displacement deformation at low voltages. The deformation is caused by an ion transport effect. The aim of this experiment was to determine whether there is a relationship between voltage and deformation for a fully hydrated IPMC strip. It was found that there is very little curvature of the strip in these conditions. A power relationship was identified to model the displacement of the strip, two linear regions were also identified. This model is important for underwater applications without a water proof surround for the IPMC. This report also covers the discovery of electroactive materials and a brief comparison between different materials is made. The production of IPMC materials and their mechanical and electronic applications are described including use as robotic grippers and actuators or for sensing delicate objects.

Keywords: *Ionic Polymer-Metal Composite, Hydrated Displacement Model*

1. Introduction

Electroactive Polymers (EAPs) are polymers that deform when subjected to a voltage, they will also generate a voltage when deformed. The first EAP was reported in 1880 by Roentgen, his experiment involved applying an electric field to a rubber band with one fixed end and hanging a mass from the other. He showed that the field was deforming the rubber band [1]. In 1925, Eguchi discovered a piezoelectric polymer, he found this electret by subjecting a cooling mixture of carnauba wax, beeswax and rosin to a DC bias field [2].

Though there are other polymers that exhibit shape changing effects, for example chemical or magnetic activation or shape memory polymers [3], the convenience and practicality of electrical stimulation led to growing interest in EAP materials. This was bolstered by the discovery in 1969 of a strong piezoelectric material, polyvinylidene fluoride (PVDF or PVF2), it was found that this compound under stress induced surface charges [4]. After these milestones, most of the advances in EAPs have been seen the in the last decade.

EAPs can be classified by the mechanism responsible for the actuation. Electronic (dry) EAPs are driven by electric field forces, whereas Ionic (wet) EAPs deform due to mobility or diffusion of ions within the composite structure. Examples of dry EAPs are ferroelectric or piezoelectric

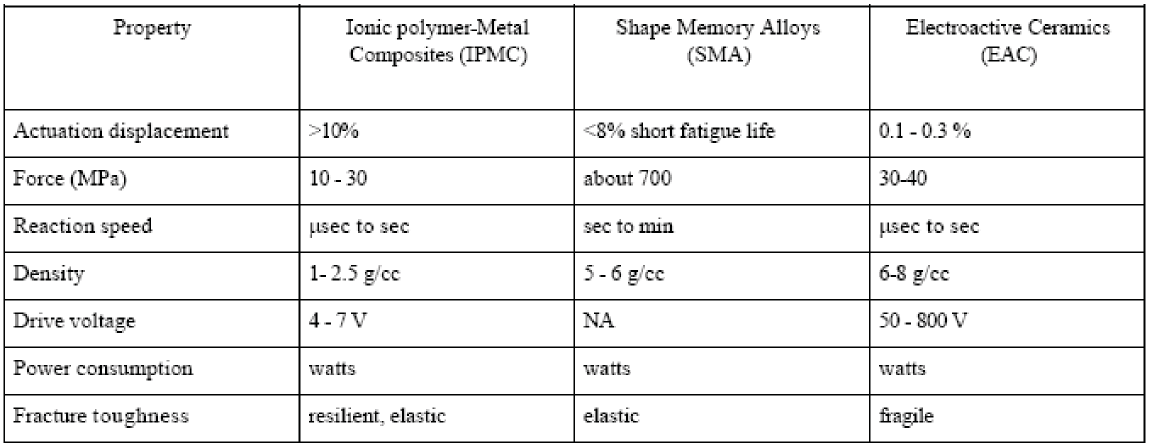

Property	Ionic polymer-Metal Composites (IPMC)	Shape Memory Alloys (SMA)	Electroactive Ceramics (EAC)
Actuation displacement	>10%	<8% short fatigue life	0.1 - 0.3 %
Force (MPa)	10 - 30	about 700	30-40
Reaction speed	µsec to sec	sec to min	µsec to sec
Density	1- 2.5 g/cc	5 - 6 g/cc	6-8 g/cc
Drive voltage	4 - 7 V	NA	50 - 800 V
Power consumption	watts	watts	watts
Fracture toughness	resilient, elastic	elastic	fragile

Figure 1. Comparison of electroactive materials [7].

materials. These EAPs usually require breakdown level activation fields (>150V/µm) though they are able to maintain the induced displacement and can be operated in air at room temperature with minor constraints. The wet EAPs are materials such as gels, ionic polymer-metal composites, conducting polymers or carbon nanotubes and are actuated at much lower voltages (1-5V). While they are capable of larger bending deformation, they are unable to hold the induced strain and will gradually restore their original shape. The materials must be operated in a wet state or in solid electrolytes and are affected by hydrolysis of water in aqueous systems [5].

The deformation mechanism of Ionic Polymers is similar to that of biological muscles, the induced strain can be designed to bend, stretch, or contract in any direction. This paper will cover Ionic Polymer-Metal Composites (IPMC). An IPMC is made up of an Ionic Polymer (IP) in composite form with a conductive medium such as a metal [5, 6].

2. Theory of the effect

The Ionic Polymer (IP) membrane consists of a network of fixed negative charges and mobile positively charged particles. In IPs, the deformation is due to the displacement of ions in the polymer.

The effect relies on two transport methods, ion transport and electrophoresis. Electrophoresis transport is the result of charged particles moving through a medium as a result of an applied electric field, in an IP these are the mobile cations. In ion transport, positive hydrated cations are attracted to a cathode. The combination of these transport effects creates a build up of cations at the cathode attracting water molecules to move to this side.

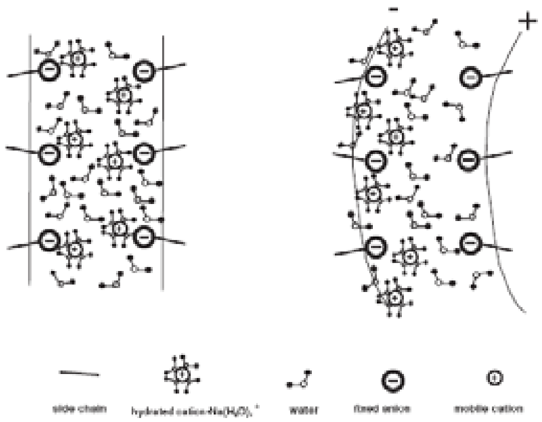

Figure 2 The transport effects causing deformation of an Ionic Polymer [Adapted from 5].

The result is hydrophilic expansion on one side, causing stresses in the polymer matrix. These stresses cause bending towards the anode, the deformation is not permanent and with time the water molecules will back diffuse causing the material to slowly relax. The deformation can be instantly reversed by changing polarity [5, 6, 8]. As part of the effect is a result of electrophoresis, the hydration level of the environment reduces the electromechanical effect, if both sides are fully hydrated the effect is drastically reduced moving slightly away from the electrodes. Deformation of the membrane can produce a voltage in a reversal of the aforementioned effect.

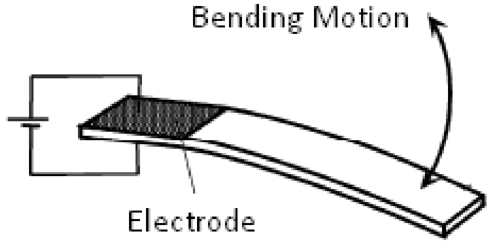

Figure 3 The bending action of an IPMC strip [Adapted from 5].

3. Current Manufacturing Technique

An IPMC strip consists of a perfluorinated ion exchange polymer composited then surface plated with metallic (commonly Platinum) ions. Therefore, IPMC preparation is a two stage process, first a compositing process, then the surface electroding process.

Ion Exchange Polymers

An ion exchange polymer is a material able to exchange ions with ionic components in a solution [9].These ionic polymers are designed to pass ions of single or multiple charges, that is cations, anions or both.

A common base material used is perfluorinated alkene, this polymer is created by a process where a substrate containing carbon bonded hydrogen is placed in a solution of hydrogen fluoride and a current is passed through. The reaction causes the hydrogen atoms to be largely replaced with fluorine atoms [10]. Side chains are then created using sulfonate or carboxylate ions.

These polymers exchange ions by a reversible chemical reaction exchanging an ion from solution for a similarly charged ion attached to a solid particle [15].

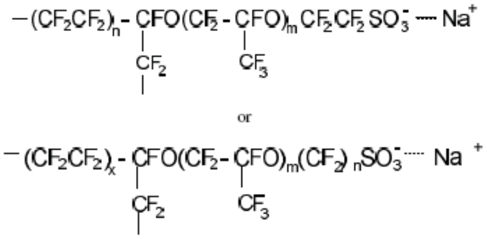

$$-(CF_2CF_2)_n-\underset{\underset{|}{CF_2}}{\underset{|}{C}}FO(CF_2-\underset{CF_3}{\underset{|}{C}}FO)_mCF_2CF_2SO_3^- \cdots Na^+$$

or

$$-(CF_2CF_2)_x-\underset{\underset{|}{CF_2}}{\underset{|}{C}}FO(CF_2-\underset{CF_3}{\underset{|}{C}}FO)_m(CF_2)_nSO_3^- \cdots Na^+$$

Figure 4 Structure of a perflourinated sulfonic acid polymer. The exchange ion in this case is Na^+[5].

Compositing

The surface of the IP is chemically composited with a conductive medium. This creates a conductive layer a few microns deep within the IP.

First the surface of the polymer membrane to be used as the electrode is roughed using a mild sandblast or sandpaper treatment. This is to increase the surface area, thus increasing the available metallic salt penetration sites. The surface is then cleaned using ultrasonic and chemical methods.

The polymer is immersed in a metal complex solution such as aqueous Platinum ($[Pt(NH_3)_4]CL_2$). The solution is then left for at least 1-3 hours. The platinum complex cations are next reduced to the metallic state by a reducing agent such as aqueous sodium or lithium borohydride at 60°C. A black layer of Platinum is deposited near the surface of the membrane.

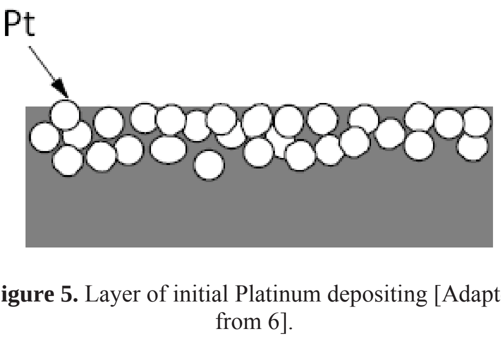

Figure 5. Layer of initial Platinum depositing [Adapted from 6].

Surface Deposition

The surface is next developed to improve surface resistivity by plating the surface of the material with more Platinum (or another noble metal). The most common method of surface deposition is by chemical reduction. An aqueous solution of the Platinum complex (concentration determines plating amount) is mixed with ammonium hydroxide, this sets the pH. The polymer is placed in the Pt solution at 40°C and 6ml of a 5% hydroxylamine hydrochloride solution is initially added with 3ml 20% hydrazine monohydrate solution added every 30 minutes. The temperature is raised to 60°C over 4 hours and grey metallic layers form on the surface. The solution can be checked for any remaining Pt by boiling a sample with a strong reducing agent, this is to ensure the initial concentration has been fully deposited. The membrane is then rinsed with water and boiled in dilute hydrochloric acid to remove the ammonium cations. The H+ in the membrane can be exchanged with another cation by washing again with water and immersing in a chloride salt of the cation [10, 11].

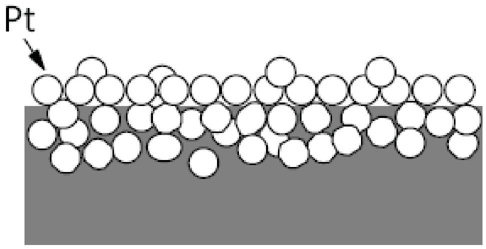

Figure 6. Second Platinum layer added to improve surface/electrode conductivity [Adapted from 6].

By altering the reduction/stirring times and cations added, electronic and mechanical properties of the IPMC can be altered, these include S/N ratio, force generated, speed and input power consumption [12].

Physical Metal Loading

A novel method of plating is also available, physical metal loading. A conductive primary powder is sprayed onto the IP membrane and pressed at 2 ton at 120°C to 130°C for 14 minutes. The particles are further secured with smaller secondary particles by chemical plating. This process also loads conductive particles into the first layer. Finally a conductive metallic layer is electroplated on top of these layers. This method is far cheaper and simpler than the chemical reduction method. This is due to the chemical method relying on noble metals (Palladium, Gold, Platinum etc) and the involved lab work [12].

4. Applications for IMPC Materials

Mechanical Applications

Gripper

A pair of IPMC strips can be used to form a mechanical gripper, similar to a pair of tweezers. The two strips can be wired to bend in and out together. Two, four and eight strip grippers have been produced. Their advantage over conventional grippers is in their inherent soft nature. This results in an ultra-dexterous and versatile end-effector. Tasks could include handling soft biological materials or planetary sample tasks, NASA/JPL has reported of possible applications even in a harsh space environment [14].

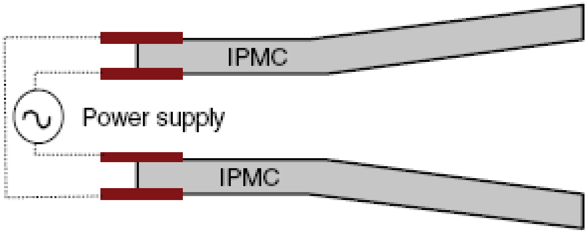

Figure 7. Tweezer configuration for a gripper [14].

Linear Actuators

A configuration of two IPMCs connected at each end can be used to produce a linear force. The IPMCs could be designed to produce the required force for the application. A platform supported IPMC strips could be controlled in multiple degrees of freedom [14].

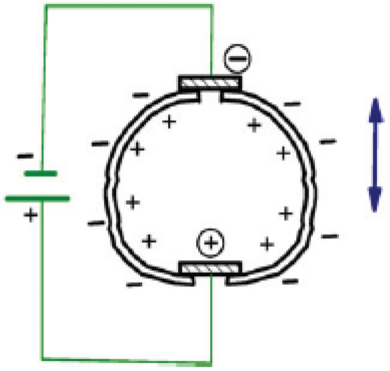

Figure 8. Deformation of the 2 strips will change the gap between the electrodes [14].

Three Dimensional Actuator.

IPMC strips can be configured as a triangular or rectangular tube. Attaching a set of electrodes at the base of each strip allows for three dimensional movement of the structure. These devices could be applied to tasks such as soft mixers or production line feeders. They could even be used as a sensor in a joystick or any X-Y locator [14].

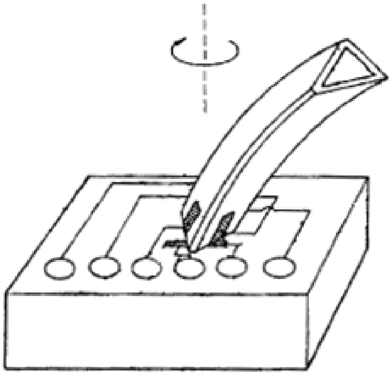

Figure 9. Three strips in a triangle configuration each controlled by electrodes at base [14].

Robotic Swimming

Applying a suitable low alternating voltage to a suitable packaged IPMC strip could produce a swimming muscle of a fish tail type. Two rows of strips could be sequentially activated for a stingray like motion. These muscles could be used in noiseless propulsion or in smart sonar evading skins. Current applications use a waterproof coating to protect the IPMC.

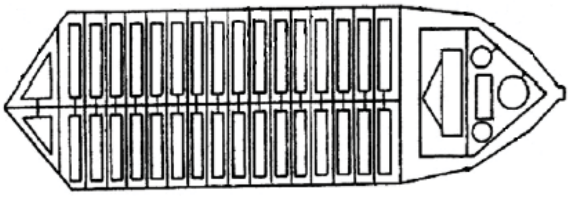

Figure 10. An IPMC fish design showing the two rows of strips [14].

Artificial Muscles

IPMCs could be used in an exo-skeleton to augment or replace human joint muscles. They could be packaged as a wearable exo-skeletal system integrated into the fabric of gloves, jackets etc. The strips are designed to fit the joint and replicate its movement. This system will improve quality of life for the disabled or improve the performance of soldier or astronauts. These devices would be able to sense joint movement then apply additional force [14].

Biomedical Applications

Cardiac Assist

IPMCs can be designed to assist with heart compression and arrhythmia control. The soft and electronically robust IPMC can be formed into a gripper or band to assist the heart. As the IPMC is implanted on the exterior of the heart it doesn’t interfere with internal blood circulation, which can cause thrombosis (blood clots) and similar complications. The device could be supported by a slender stem allowing the heart to continue its systolic and diastolic cycles without restriction. The device would assist the left ventricle of a weak heart to increase internal pressure and pump blood from one or more sides to match the natural rhythm. Electrodes can be included to monitor the heart and improve arrhythmia control [14].

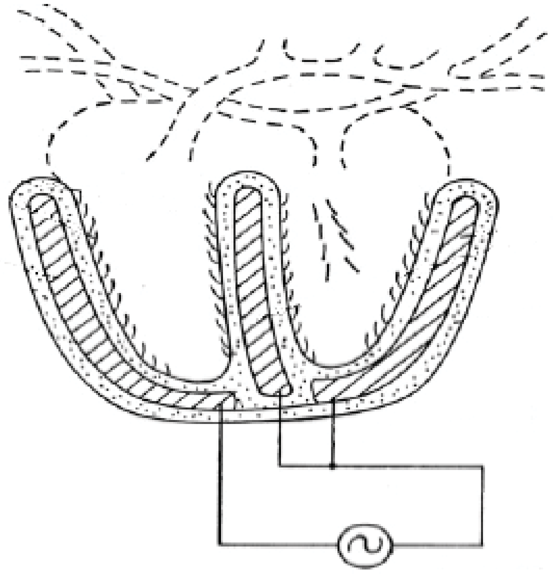

Figure 11. The cardiac assist IPMC at bottom attached to the heart [14].

Pump

A diaphragm (bellows) pump can be made by attaching two planar strips across a cavity. By varying the frequency and voltage the flow can be adjusted. These pumps could be used to drain bodily fluids or dispense drugs in the body. The device could be powered transcutaneously by biocompatible inductive coils or by another IPMC attached to a local bending or twisting force [14].

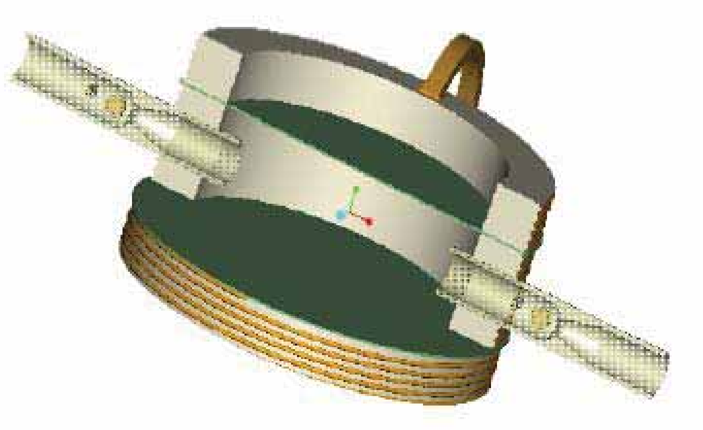

Figure 12. Model of an IPMC diaphragm pump [14].

Tactile Display

An array of IPMCs could be configured to provide tactile feedback. This would help human dextrous telemanipulation in fields such as medicine, space or other extreme environments. There are also applications for virtual reality. The display relays information such as roughness and friction of a material [15].

Biomimetic Sensing

Deformation of the strip will produce a voltage gradient, this can easily sensed by a low power amplifier [7]. The soft material will not damage the object and the lightweight simple nature makes for small devices. The IPMC could even be wired in such a way to switch between sensing and actuating functions. This could also be achieved by separating the sensing and actuating parts of a strip with grooves.

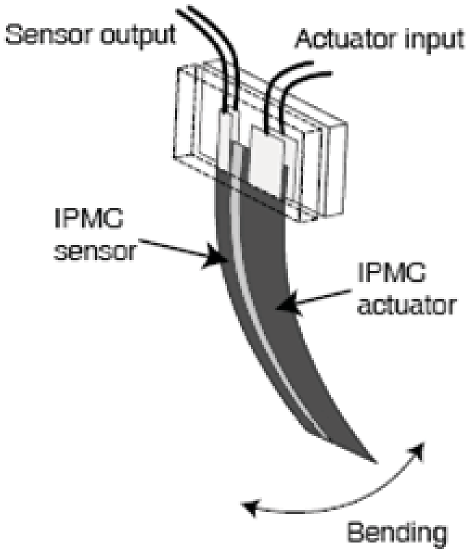

Figure 13. A combination sensor and actuator IMPC design [Adapted from 13].

Quasi-Static Sensing

A quasi-static process is one that happens infinitely slowly, but can be approximate by performing the experiment very slowly. It was shown [7] that there exists a linear relationship between voltage and displacement.

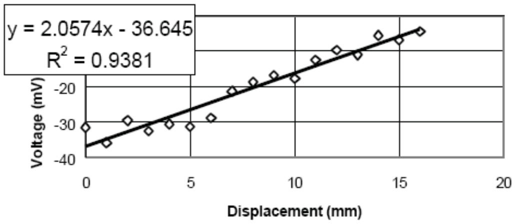

Figure 14. Sensor response for displacement input [7].

Dynamic Sensing

An IMPC strip subjected to impact or shock loading was found to produce a damped response. This response was found to be highly repeatable up to 100’s of Hz. It has also been shown [15] that the velocity of displacement is directly related to the voltage produced. This sensing could be applied to large motions in many industrial applications.

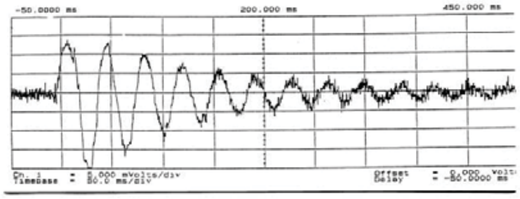

Figure 15. IMPC damped electrical response to impact loading as a cantilever [7].

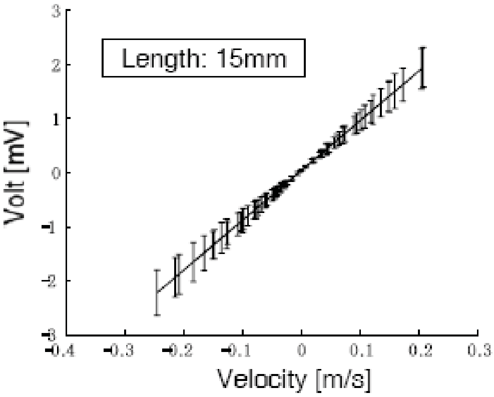

Figure 16. Relationship between sensing response and velocities [15].

Microelectromechanical Systems

Microelectromechanical systems (MEMS) are the integration of mechanical elements, sensors, actuators and electronics on a common silicon substrate [14]. IPMCs can replace the electroceramics and shape memory alloys currently used in MEMS. IPMCs are lighter and exhibit superior properties to these materials, higher striction and faster response, respectively. IPMCs can be manufactured to any desired shape for use in these micro actuators and sensors.

MEMS are an extremely diverse technology that could significantly impact on every category of product. As MEMs and IPMCs are manufactured in a batch process they can be mass produced at relatively low cost [14].

5. Fully Hydrated IPMC Operation

The study of fully hydrated IPMC operation is required for underwater or wet environments. Many published papers create their device then record data on how it works, rather than collect data on the IPMC material itself. The IPMC specimen used in this investigation was provided by ERI, Inc.

Apparatus

The IPMC was in the form of a strip approx 10x50mm and 1mm thick. The strip was held in a tray of de-ionised water by the electrode mount. The mount was provided by Sean Manley, a Masters student in the Department of Mechanical Engineering, an aluminium frame with screw tightened electrodes to hold the strip in place. The images were captured using a Conex camera.

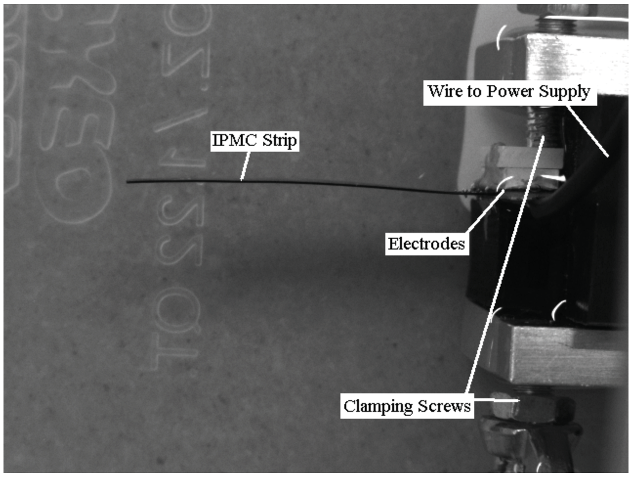

Figure 17. Experimental Apparatus

The aim is to obtain an equation showing the relationship between voltage and displacement. This is achieved by measuring the deflection of the strip for successive voltage levels of ~0.5v from 1v to 6.5v. A reference image is captured at zero volts before every volt step. The voltage was applied as a step input and the image was captured as the strip reached maximum displacement and before the strip began to relax. The voltage was then set to zero and the strip allowed time to relax to the initial position, this taking approx 1-2 minutes. It was found that after recording the full range of inputs and returning to lower potentials, the deformation of the strip is lessened when repeating the experiment.

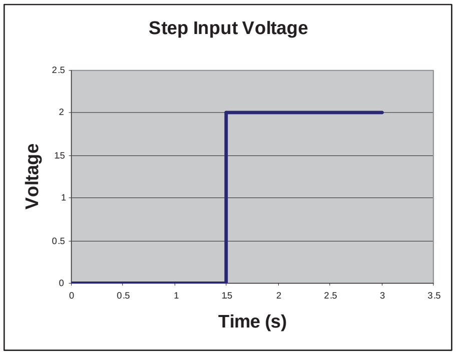

Figure 18. Input to electrodes.

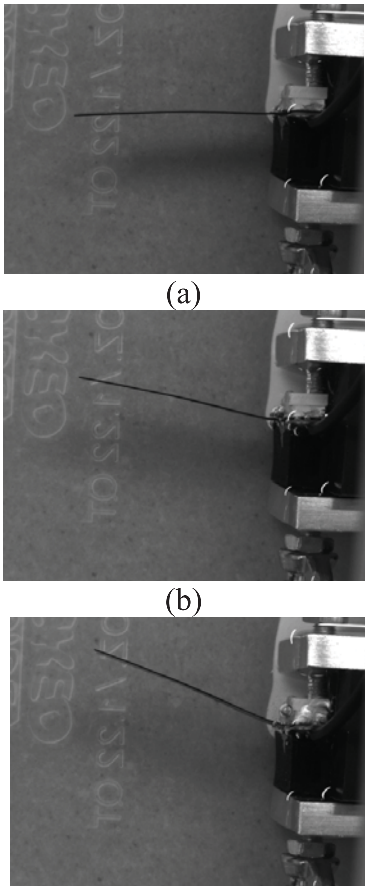

(a)

(b)

(c)

Figure 19. Images captured at (a) 0v, (b) 3.5v and (c) 6.5v.

It is clear that the deformation curvature is greatly reduced under full hydration when compared with a typical IPMC actuated in the air. This is in stark contrast to the example shown in Figure 20 with only a 3V potential applied.

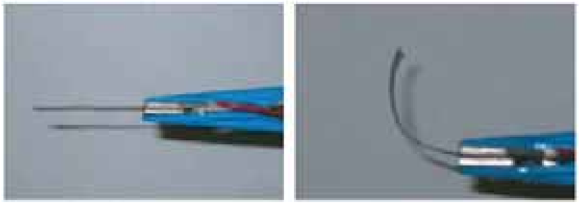

Figure 20. Typical IPMC deformation at 3V in room temperature air [16].

The difference was so much that a composite image was created to check this using images from the 6.5V step. One image was then rotated to align the base of the strip. It is revealed that there is very little curvature even at the highest voltage applied.

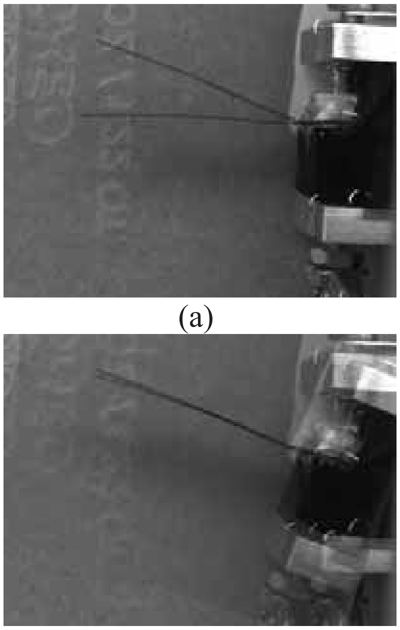

(a)

(b)

Figure 21. (a) Original composite image, (b) second image rotated to show lack of curvature.

6. Results

The images were analysed using InSight software. Due to the slight curvature of the overall strip, it was decided the radius of the first approx 10mm and the overall deflection of the strip would be found.

Deflection Radius

The Insight software enables us to find a curve or edge within a specified region. However, the region must be manually set up to follow the curvature of the line. A single region could not be used to capture all the radii required. The radii were retrieved multiple times and averaged, the result shown in Figure 22. The averaged data shows a power relationship, however, two distinct regions can be identified, above and below 3.5 V, with close to linear relationships.

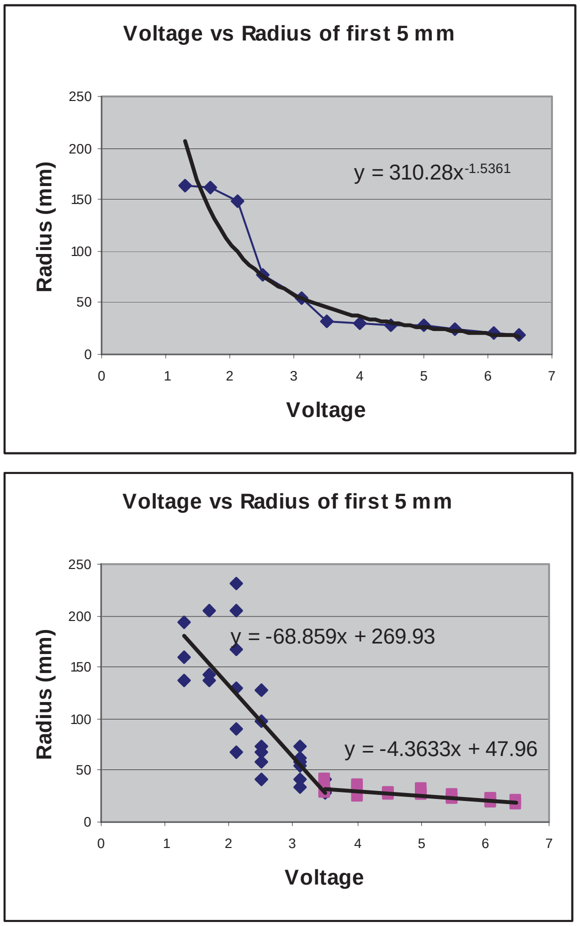

Figure 22. Voltage vs Radius plots used to find relationships (Top) Power Relationship from the Averaged Data, (Bottom) Linear Relationship from Raw data.

Deflection Angle

Of greater interest was the overall deflection of the strip, this was easier to obtain by directly taking the pixel counts of the images and converting to deflection angle. Two distinct regions can be identified, their linear relationships to voltage are shown in Figure 23.

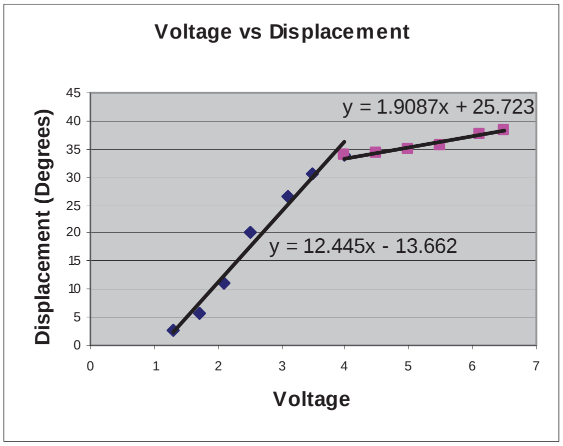

Figure 23. Voltage vs Displacement Angle in Degrees.

7. Discussion

Data from Shahinpoor et al [7] for actuation in air was also converted to angle for comparison. Shahinpoor et al applied a voltage at 0.5 Hz with strip size 5mm x 0.2mm x 20mm, their results are shown in Figure 24.

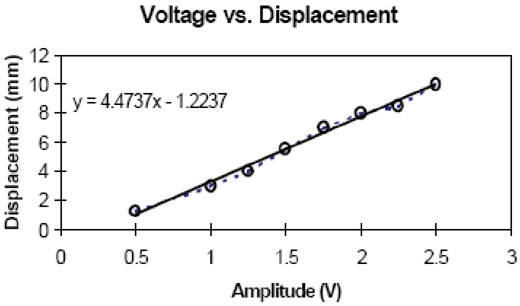

Figure 24. Relationship found by Shahinpoor et al [7] for displacement (mm) in air.

Using the trend from Figure 24 and dimensions of the IPMC used, the displacement angle was calculated to compare with the fully hydrated data for voltage ≤ 4 V. The overlapping voltage range from the two data sets are compared in Figure 25.

The trend curves have surprisingly similar gradients, it is clear the hydrated operation requires a higher voltage to reach the same angle. The raw data from both sources shows a similar 'S' shape. The increased voltage required is likely due to the fact that upon applying a current, the hydrated cation depleted side of the IPMC is being replenished by the hydrated environment.

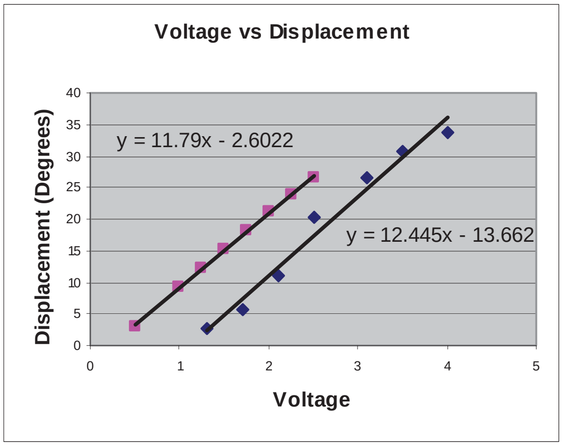

Figure 25. Comparison with data from [7] at left and fully hydrated data at right.

This would imply the effect is relying largely on electrophoresis transport and that the ion transport effect is reduced. Observations made by Shahinpoor et al [7] showed that water content has quite an effect on the deformation of the strip in air. Above 2 volts they observed reduced displacement and electrolysis of the water contained within the IPMC strip. This prompted them to completely swell the strip before each experiment. An issue which may be difficult to overcome if IPMCs are not used in a hydrated environment, this is shown in their robotic fish using polymer coated IPMCs having degraded performance over time. This coating also reduced the displacement amplitude of the strip. These observations show how important it is to model the IPMC in a fully hydrated state. Further testing may result in a similar degradation while hydrated, though it would be expected to be lessened. The effect of cations in the water was not covered in this experiment, as de-ionised water was used.

Kwang et al [16] performed a study of IPMC operation in saltwater, though their method applied a cyclic voltage only covering a small range of -0.4v to 1.2v, essentially applying a 1.6v potential to the resulting cyclic displacement of the strip is seen in Figure 26.

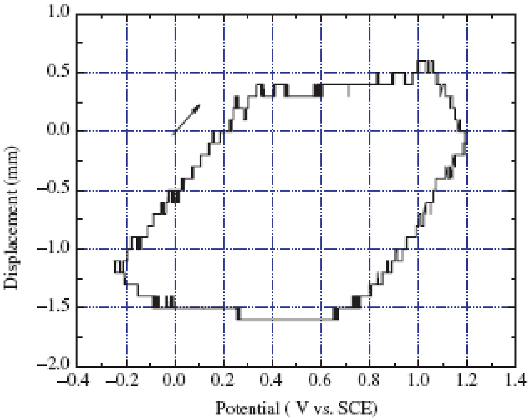

Figure 26. Voltage vs displacement in mm for cyclic loading of an IPMC strip in saltwater [16].

Their data shows an approximately 2mm displacement range for the 1.6v potential which is similar to the results obtained in this report, as can be seen in Figure 27 for a 1.6v input.

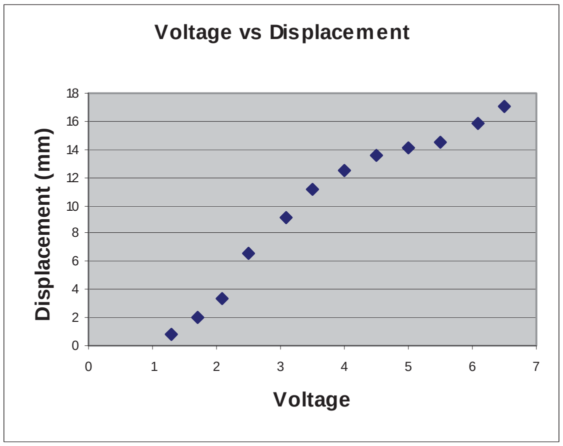

Figure 27. Voltage vs Displacement in mm for IPMC strip in de-ionised water.

As the input used in this experiment was a step input voltage, it should be noted that Shahinpoor has also experimented with varying the frequency of a 1.5v potential as a sine wave input [17]. He found that as the frequency increased, the maximum deformation in both directions decreased as shown in Figure 28.

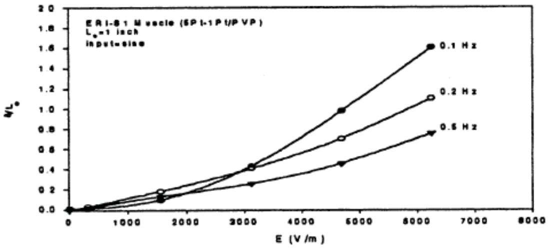

Figure 28. Displacement vs Voltage to a 1.5v sine input, the trends from top to bottom are at 0.1Hz, 0.2Hz and 0.5Hz [17].

Shahinpoor also showed that in response to a step input there was an initial larger displacement, after which the strip relaxed back to a steady state position after 10 seconds, Figure 29.

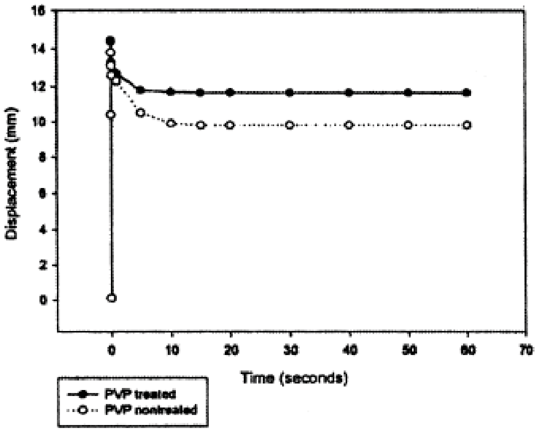

Figure 29 Actuation under a step voltage [17].

These deformation properties, when combined with the sensing characteristics provided by [7], shown in Figure 14, could be used as a closed loop feedback system. This system would consist of pair of IPMC strips, one as sensor, and one as actuator, to achieve a desired position. However, due to the relaxing back effect, this perhaps should only be applied in areas where a brief force or movement is required. The reduced degradation of fully hydrated performance is promising for underwater, long-lasting applications as only a slightly higher voltage is required to achieve the same result.

8. Conclusions

This report discussed the fundamentals of Ionic Polymer Metal Composites. The explanation of the Ionic Polymer transport was given and the IPs compared to other electroactive polymers. The production of IPMC materials, a chemical reduction process, was described. The useful properties of IPMC materials such as softness, lightweight and large fast deformation for a low activation voltage can be applied to many fields. Potential applications for the mechanical and sensing properties of IPMCs were given. A relationship between voltage and displacement was discovered, as well as a relationship to curvature. This was compared to other similar research. It was also found that the deformation shape was much less curved for a hydrated IPMC strip than for one actuated in dry air. It is clear that more research into the properties of IPMC materials in different environments is required before many of the exciting applications are taken on.

Acknowledgements

The results of this report were obtained under the supervision of Dr K.C. Aw. Experimental apparatus was provided by Mr Sean Manley and the IPMC material was purchased from ERI, Inc.

References

1. Roentgen, W.C. (1880) “About the changes in shape and volume of dielectrics caused by electricity,” Section III in G. Wiedemann (Ed.), Annual Physics and Chemistry Series, **11**, 771-786,.(In German)
2. Eguchi, M. (1925), *Phil. Mag.*, **49**, 178.
3. Yoseph Bar-Cohen (2003) “Actuation of biologically inspired intelligent robotics using artificial muscle”, Industrial Robot: An International Journal. **30**, 331-337.
4. Kawai, H. (1969) “The Piezoelectricity of Poly(vinylidene Fluoride)”, Jpn. J. Appl. Phys. , **8**, 975-97
5. Kim K. J. Ionic Polymer-Metal Composite as a New Actuator and Transducer Material. In Kwang J. Kim and Satoshi Tadokoro (Eds.), Electroactive Polymers for Robotic Applications - Artificial Muscles and Sensor (Chapter 6). Springer-Verlag London Limited 2007
6. Mohsen Shahinpoor and Kwang J Kim (2001) “Ionic polymer–metal composites: I. Fundamentals”, Smart Materials and Structures. **10**, 819–833
7. M. Shahinpoor, Y. Bar-Cohen, T. Xue, J.O. Simpson and J. Smith. Ionic Polymer-Metal Composites (IPMC) As Biomimetic Sensors and Actuators. Proceedings of SPIE's 5th Annual International Symposium on Smart Structures and Materials, 1-5 March, 1998, San Diego.
8. Electrophoretic. Retrieved 2nd October 2008 from http://www.thefreedictionary.com/electrophoretic.
9. Ion Exchange Polymer. Retrieved 2nd October 2008 from http://www.iupac.org/goldbook/IT07155.pdf
10. Electrochemical fluorination using interrupted current. United States Patent 6267865
11. Ion Exchange. Retrieved 2nd October 2008 from http://www.remco.com/ix.htm
12. Mohsen Shahinpoor and Kwang J Kim (2003) “Ionic polymer–metal composites: II. Manufacturing techniques”, Smart Materials and Structures. **12**, 65-79
13. Preparation Procedure Ion-Exchange Polymer Metal Composites (IPMC) Membrane. http://ndeaa.jpl.nasa.gov/nasa-nde/lommas/eap/IPMC_PrepProcedure.htm
14. Mohsen Shahinpoor and Kwang J Kim (2003) “Ionic polymer–metal composites: IV. Industrial and medical applications”, Smart Materials and Structures. **14**, 197-214
15. Konyo M, Tadokoro S, Asaka K. Applications of Ionic Polymer-Metal Composites : Multiple-DOF Devices Using Soft Actuators and Sensors. In Kwang J. Kim and Satoshi Tadokoro (Eds.), Electroactive Polymers for Robotic Applications - Artificial Muscles and Sensor (Chapter 9). Springer-Verlag London Limited 2007
16. Kwang J. K, Woosoon Y, Jason W. P, Doyeon K (2007) “Ionic Polymer-metal Composites for Underwater Operation”, Journal of Intelligent Material Systems and Structures,**18**, 123 – 131.
17. Shahinpoor M (2003) “Ionic polymer-conductor composites as biomimetic sensors, robotic actuators and artificial muscles”, Electrochimica Acta, **48**, 2343-2353.